Universidade de São Paulo
Instituto de Física

Projeto conceitual de um sistema de bobinas RMP para o tokamak TCABR

Felipe Machado Salvador

Orientador: Prof. Dr. Gustavo Paganini Canal

Dissertação de mestrado apresentada ao Instituto de Física da Universidade de São Paulo, como requisito parcial para a obtenção do título de Mestre(a) em Ciências.

Banca Examinadora:
Prof. Dr. Gustavo Paganini Canal - Orientador (IFUSP)
Prof. Dr. Diego Sales de Oliveira (École Polytechnique Fédérale de Lausanne - Suíça)
Prof. Dr. Vinícius Njaim Duarte (Princeton Plasma Physics Laboratory - EUA)

São Paulo
2022

FICHA CATALOGRÁFICA
Preparada pelo Serviço de Biblioteca e Informação do Instituto de Física da Universidade de São Paulo

Salvador, Felipe Machado

Projeto conceitual de um sistema de bobinas RMP para o tokamak TCABR. São Paulo, 2022.

Dissertação (Mestrado) – Universidade de São Paulo. Instituto de Física. Depto. de Física Aplicada

Orientador(a): Prof. Dr. Gustavo Paganini Canal

Área de Concentração: Física de Plasmas

Unitermos: 1. Magnetohidrodinâmica; 2. Equilíbrio e estabilidade MHD; 2. Tokamak; 3. Física de plasmas

USP/IF/SBI-056/2022

University of São Paulo
Institute of Physics

Conceptual design of a system of RMP coils for the TCABR tokamak

Felipe Machado Salvador

Supervisor: Prof. Dr. Gustavo Paganini Canal

Dissertation submitted to the Institute of Physics of the University of São Paulo in partial fulfilment of the requirements for the degree of Master of Science.

Examining Committee:
Prof. Dr. Gustavo Paganini Canal - Supervisor (IFUSP)
Prof. Dr. Diego Sales de Oliveira (École Polytechnique Fédérale de Lausanne - Suíça)
Prof. Dr. Vinícius Njaim Duarte (Princeton Plasma Physics Laboratory - EUA)

São Paulo
2022

Agradecimentos

Dedico este trabalho à minha família: Cátia, Sérgio Ricardo e Tiago. Sem dúvidas, o apoio familiar foi fundamental para que este trabalho pudesse ser realizado em meio à pandemia da COVID-19. Sou extremamente grato aos meus amigos Leonardo Barreto, Vitor Cavalheri, Rafael Spaziani, Giancarlo Tosto, Vitor Hugo Figueira, Giovana Shimoda, Lucas Proença, Júlia Felix, Lucas Nogueira, Giovanna Verrillo e Gabriel Ruiz pela amizade, camaradagem, risadas e apoio durante essa jornada.

Agradeço também a Dmitri Orlov e Andreas Kleiner por terem me ajudado no desenvolvimento deste projeto com extrema solicitude e paciência. Sou muito grato aos meus amigos e colegas de trabalho André Bouzan e Yuri Asnis, por suas contribuições na minha pesquisa por meio de sugestões, discussões e disponibilidade para ajudar nos problemas.

Por fim, agradeço, do fundo de meu coração, ao meu orientador Prof. Gustavo Canal por me aceitar nesse mestrado e por todas as nossas conversas e ajudas que nesse projeto foram essenciais para a realização deste.

O presente trabalho foi realizado com apoio do CNPq, Conselho Nacional de Desenvolvimento Científico e Tecnológico - Brasil.

We fly like a feather
So immune and free.

Nataliia Zhyzhchenko (ONUKA), *19 84*

I have to keep going to find out ultimately what is the matter with it in the end.

Richard Feynman, *Surely You're Joking, Mr. Feynman*

Abstract

The high confinement mode observed in tokamak plasmas is seen as the most promising operational regime for economically viable nuclear fusion power plants. A particular characteristic of the high confinement plasmas is the onset of periodic instabilities known as edge localized modes (ELMs). These instabilities generate unacceptably large heat fluxes on the divertor plates that erode the divertor and reduces significantly its life time on a future reactor. Therefore, there is a need to develop ELM control methods in large machines, such as ITER. Several experiments have demonstrated that the application of non-axisymetric resonant magnetic perturbations (RMPs), created by electric currents flowing in localised coils outside the plasma, can be used to control ELMs. Due to its efficiency, ELM control coils, also called RMP coils, were added to ITER baseline project. Although the RMP coils have been successfully used to suppress ELMs in various tokamaks, the numerical modelling of these plasma discharges reveal that current physical models are not capable of describing satisfactorily the observed effects. The lack of a trustworthy physical model to describe the impact of RMP fields in tokamak plasmas is a central topic when plasma physics scientists try to predict the plasma reaction to the RMP fields in ITER. In order to enhance the numerical results reliability, carefully designed experiments to validate physical models are being realised in several tokamaks around the globe. Here in Brazil, a significant upgrade of the TCABR tokamak, operated at Plasma Physics Laboratory of Institute of Physics of the University of São Paulo, is in progress. In this upgrade, it is planned the installation of six sets of RMP coils, which enable the TCABR to test physical models used to predict the plasma response to RMP fields. This work has the objective of designing the RMP coil sets that will be installed in TCABR, which enables the validation of physical models in a wide variety of plasma scenarios, RMP field configurations and magnetic spectra with a large range of poloidal and toroidal harmonics.
Keywords: Magnetohydrodynamics, MHD equilibrium and stability, Tokamaks, Plasma Physics.

Resumo

O modo de alto confinamento observado em plasmas de tokamaks é visto como o regime operacional mais promissor para se obter usinas de energia a fusão nuclear economicamente viáveis. Uma característica particular desses plasmas de alto confinamento é a presença de instabilidades periódicas conhecidas como *edge localized modes* (ELMs). Estas instabilidades causam fluxos de calor inaceitavelmente altos nas placas do divertor de modo que a erosão causada por tal fluxo reduzirá significativamente o tempo de vida do divertor em um futuro reator. Há, portanto, a necessidade de desenvolver métodos de controle de ELMs em máquinas de grande porte, como o ITER. Tem sido amplamente demonstrado que a presença de perturbações magnéticas ressonantes (*resonant magnetic perturbations* - RMPs) não-axissimétricas, criadas por correntes elétricas fluindo em bobinas localizadas fora do plasma, podem ser usadas para suprimir ELMs. Devido à sua eficiência, bobinas de controle de ELMs, comumente chamadas de bobinas RMP, foram adicionadas ao projeto base do ITER. No entanto, embora tais bobinas têm sido usadas com sucesso para suprimir ELMs em vários tokamaks, a modelagem numérica dessas descargas revela que os modelos físicos atuais ainda não são capazes de reproduzir satisfatoriamente os efeitos observados. A falta de um modelo físico confiável que descreva o impacto de campos RMP em plasmas de tokamak é uma questão fundamental quando se tenta prever a resposta de plasmas criados no ITER à campos RMP. Para melhorar a confiabilidade dos resultados destes códigos, experimentos cuidadosamente projetados para validar modelos físicos estão sendo realizados em vários tokamaks ao redor do mundo. Aqui no Brasil, um upgrade significativo do tokamak TCABR, operado pelo Laboratório de Física de Plasmas do Instituto de Física da Universidade de São Paulo, está em andamento. Neste upgrade, está planejado a instalação de seis conjuntos de bobinas RMP que permita a criação de ambientes no TCABR em que os modelos físicos usados para prever a resposta de plasmas à campos RMP possam ser validados. Este trabalho tem como objetivo projetar o sistema de bobinas RMP que será instalado no tokamak TCABR. As bobinas RMP serão projetadas de modo a permitir a validação de modelos físicos em uma ampla variedade de cenários de plasma, de configurações geométricas de campo RMP e de espectro com amplo conteúdo de harmônicos toroidais e poloidais.
Palavras-chave: Magnetohidrodinâmica, Equilíbrio e estabilidade MHD, Tokamak, Física de Plasmas.

List of Figures

Contents

Chapter 1

Introduction

For decades, scientists have been working to establish conditions in which controlled thermonuclear fusion become economically viable in order to enable this energy source to be part of the energetic matrix. In this chapter, the main challenges encountered in the development of nuclear fusion power plants are discussed.

1.1 The need for new energy resources

Energy is the most basic need for food production, heating, lighting, transport, etc. In order to maintain a high quality of life, a substantial energy demand needs to be supplied by low-cost energy generation. The increase of the quality of life of the world population, along with a significant raise in population, has led to a boost in energy usage. International agencies expect a world energy consumption increase of, approximately, 56% in the period between 2010 and 2040 [3, 4]. The major contribution to this raise (more than 85%) is caused by the economic and population growth on emerging countries, such as China and India. One of the biggest challenges in meeting this rising energy demand is to find new energy sources which are safe, environmentally sustainable and economically viable. The present energy demand is supplied by a combination of several resources, such as fossil fuels, solar, wind, hydroelectric, nuclear fission and geothermal. Each options has its benefits and hindrances, hence there is no unique and obvious solution to the problem. The majority of the countries uses fossil fuel power plants to power their homes and industries.

In principle, the energy demand rise can be addressed by an increase in coal burning, of which reserves are quite substantial - they can meet the present energy consumption at the current rate for several centuries [5]. However, the CO_2 emission during the burn of fossil fuels is starting to cause observable negative effects in the environment and climate. The apparent scientific consensus is that this solution is highly disfavourable for the humanity. The necessity of the reducing the emission of greenhouse gases, such as CO_2, shows that the energy production through fossil fuel burning needs to be limited. However, there are only few scenarios in which fossil fuels are totally substituted by other energy sources that causes less damage to the environment. Hence, in the absence of a solution, alternative energy sources must be investigated and developed.

1.2 Thermonuclear fusion and magnetic confinement

Nuclear fusion is one of the very few envisaged energy sources that has the potential to be part of the energetic matrix. For nuclear fusion to occur, the electrostatic repulsion between two positively charged atomic nuclei must be overcome. Therefore, high kinetic energy nuclei are needed in this process. Among the possible exothermic nuclear reactions, the most prominent is the one that involves two hydrogen heavy isotopes Deuterium (D) and Tritium (T):

$$ {}_1\mathrm{D}^2 \quad + \quad {}_1\mathrm{T}^3 \quad \longrightarrow \quad {}_2\mathrm{He}^4\,(3.50\ \mathrm{MeV}) \quad + \quad {}_0\mathrm{n}^1\,(14.1\ \mathrm{MeV}). \tag{1.1} $$

This reaction has the largest cross section at the lowest activation energy [6, 7]. Nonetheless, the largest value of this reaction cross section is still much smaller than the cross section associated to a Coulombian scattering. As a consequence, a nucleon will be scattered by other nuclei several times before a D-T reaction happens, even though the nuclei have sufficient kinetic energy to fuse. Hence, nuclei must stay confined for a sufficiently long time for nuclear fusion reactions to have time to happen. The most promising solution for this condition is heating a mixture of D and T until their temperature is high enough for the nuclear fusion processes. Due to the thermal nature of this processes, it is called thermonuclear fusion. In order to maintain the high temperature required for nuclear fusion to take place, the contact between particles and material walls must be minimised. At such temperatures, atoms are totally ionised and, hence, they are on the plasma state. Since electric charged particles are influenced by electromagnetic fields, a potential plasma confinement method is using magnetic fields.

Different magnetic configurations for fusion have been proposed, with several geometric field configurations. At the 1950's, a magnetic confinement concept called *tokamak* was developed to study energy production conditions through thermonuclear fusion [8]. The word *tokamak* is a Russian acronym for ***to****roidalnaja* ***ka****mera s* ***ma****gnitnymi* ***k****atushkami*, which can be translated as toroidal chamber with magnetic coils. The plasma temperature achieved on this first tokamak was much higher than those obtained at other concepts [9]. For this reason, research on tokamaks grew at a fast pace. Nowadays, the tokamak is still the most developed concept for thermonuclear plasmas studies and, therefore, is the most advanced candidate for a future nuclear fusion power plant.

1.3 The physics of tokamak plasmas

In future fusion power plants, the major contribution to keep the plasma temperature must come from the fusion-born α particles. The energy transfer from the α particles to D and T is done through Coulomb scattering. Therefore, it is vital that α particles be sufficiently well confined for their confinement be long enough so they transfer the majority of their energy (3.5 MeV) to the plasma. For a future fusion power plant to be economically viable, the plasma energy must be confined for a sufficiently long time in order to auxiliary heating, needed to keep the plasma at the desirable temperature, be minimal. This energy balance is expressed in terms of the energy confinement time, τ_E, which is defined as the ratio of the total plasma thermal energy and plasma power losses.

When the energy produced by D-T reactions is equal to the energy needed to keep the plasma at a specific temperature, it is said the plasma reached the breakeven condition. At this state, the energy released by fusion is equal to the energy lost by the plasma. This condition can be expressed by the Lawson criterion [10], also known as the triple product:

$$n_0 \, T_0 \, \tau_{\mathrm{E}} \; > \; 3 \times 10^{21} \, \frac{\mathrm{keV} \cdot \mathrm{s}}{\mathrm{m}^3}. \tag{1.2}$$

Here n_0 and T_0 are the maximum values for the ion density and temperature, whose profile shape are parabolic. This condition shows the requirements for the plasma density, temperature and energy confinement time to reach the breakeven condition. The Lawson criterion can also be expressed in terms of the fusion energy gain factor, Q, defined as the ratio of the produced fusion power and the auxiliary heating power needed to keep the plasma at a stationary state. When the plasma reaches $Q = 1$, the plasma is said to be in the breakeven. In practice, however, the α particle confinement is not perfect and part of the particle energy is inevitably lost to material walls. Hence, if the auxiliary heating is turned off, a $Q = 1$ plasma starts to cool-down and it exits from the $Q = 1$ state. As Q is past the breakeven condition, self-heating increases and gradually relaxes the need for auxiliary heating. When $Q = \infty$ happens, the reaction becomes self-sustained and this condition is called ignition. Operation just below ignition condition is highly desirable for future fusion power plants.

1.4 The objectives of this work

This thesis aims to contribute toward solving two important thermonuclear fusion problems: (*i*) the plasma stability of the standard high confinement mode TCABR plasma and (*ii*) the validation of physical models that describe the plasma response to non-axisymmetric externally applied resonant magnetic perturbation (RMP) fields. The motivations for each topic are given in subsections 1.4.1 and 1.4.2.

1.4.1 The threads posed by plasma edge instabilities

Many scientific challenges must be surpassed before nuclear fusion becomes a economically viable energy source. Instabilities in plasma are still a concern as they impose several and complex restrictions to the maximum device performance. Edge plasma instabilities showed to be a threat in the development of fusion power plants with plasmas operated in the high confinement mode, also called H-mode. This confinement mode is seen as the most promising operational regime for the construction of economically attractive fusion power plants. This regime is characterised by the formation of a high pressure gradient in the plasma edge and by the development of instabilities known as edge localised modes (ELMs) [11]. ELMs were identified as *peeling-ballooning* modes, triggered by the increased pressure gradient and/or the current density in the plasma edge [12, 13, 14, 15]. The crash of these modes transports a significant part of the plasma thermal energy to a region around the plasma called scrape-off layer (SOL) in which the ejected energy is carried to the first walls. This energy transport creates unbearable levels of heat flux onto

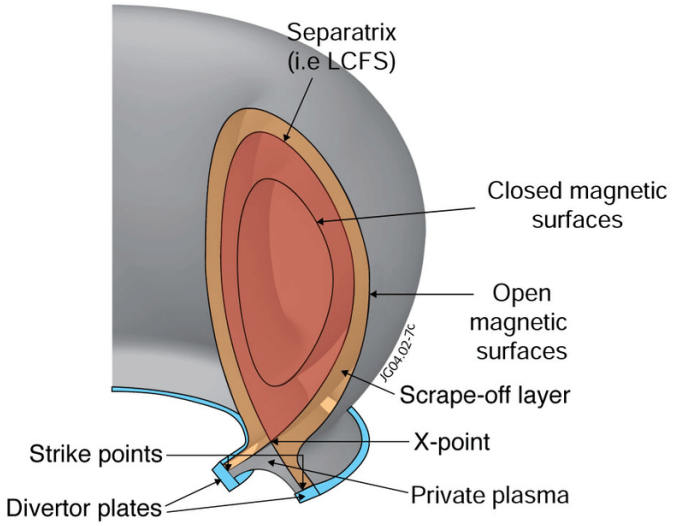

Figure 1.1: Schematic draw of a tokamak plasma with a divertor.

the divertor plates [16], Figure 1.1. The erosion caused by the high heat fluxes onto the divertor plates can decrease the plasma facing component (PFC) lifespan severely. Consequently, the development of ELM control strategies is crucial to enable the development of fusion power plants.

Several studies showed that the application of RMP fields, created by electric currents circulating in coils outside the plasma, affects ELM behaviour [17]. These perturbations reduces drastically, and sometimes completely suppresses, the transient heat fluxes caused by ELMs, replacing an intermittent wall heat load by an approximately constant wall heat load. The explanation for the observed ELM suppression through the use of RMP fields is the enhancement of plasma radial transport in plasma edge by the creation of a stochastic layer, limiting the increase of the pressure gradient in the plasma edge and preventing the plasma from entering into an unstable region of the operational space. In order to create a stochastic layer, magnetic islands must be created at rational surfaces located in the plasma edge and these magnetic islands must overlap with those at neighbouring flux surfaces.

Due to their efficiency, ELM control coils, also termed as RMP coils, were incorporated to the base project of the *International Thermonuclear Experimental Reactor* (ITER)[18, 19] to control ELMs. ITER is a experimental reactor which is being constructed at Saint-Paul-lès-Durance, France, through consortium of countries formed by European Union, India, Japan, China, Russia, South Korea and the United States of America. The ITER cross-section is shown in Figure 1.2.

Although the use of RMP coils proved to be successful in mitigating/suppressing ELMs in various tokamaks around the globe, numerical modelling of these discharges shows that present physical models are still not capable of reproducing quantitatively the observed effects. A trustworthy physical model that can describe satisfactorily the plasma response to RMP fields is vital to the prediction of plasma response of ITER plasmas to RMP fields. In order to enhance the predictions reliability of physical models, carefully

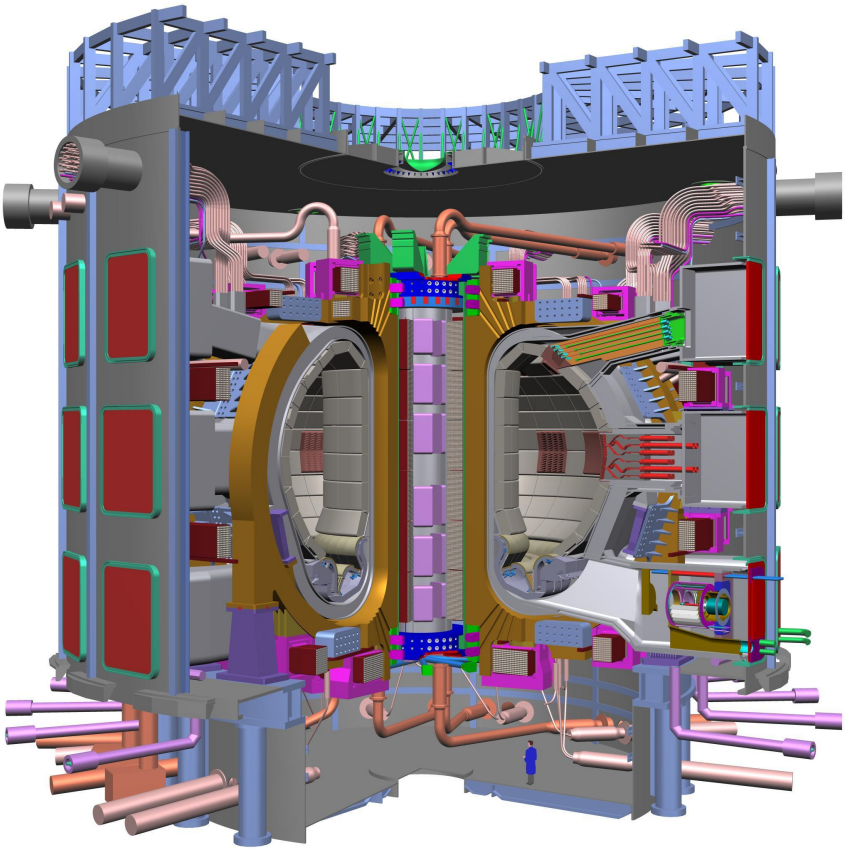

Figure 1.2: Cross section view of the ITER tokamak

projected experiments to validate these models are being carried in tokamaks around the world. Here, in Brazil, a significant upgrade of the *Tokamak à Chauffage Alfvén Brésilien* (TCABR) is in progress. TCABR is a small tokamak operated at the Plasma Physics Laboratory of Institute of Physics of the University of São Paulo. The ultimate goal of this upgrade is to install an innovative set of RMP coils that will enable TCABR to create plasma scenarios in which physical models, used for predicting the plasma response to RMP fields, can be validated in conditions not achieved in other current tokamaks.

1.4.2 The impact of RMP fields on ELMs

In order to control ELMs, some techniques were developed and tested in tokamaks. The first technique that mitigated ELMs was the use of poloidal field coils in TCV and ASDEX Upgrade. This technique consists of the application of square voltage perturbations to the poloidal field coils, making the plasma oscillate vertically. The results showed that ELMs, in both TCV and ASDEX Upgrade, were mitigated and the peak heat fluxes onto the divertor decreased [20, 21]. A different method to control ELMs is the repetitive pellet injection, tested in ASDEX Upgrade. The results showed that, for adjusted pellet size and velocity, the pellets triggered ELMs, whose peak heat fluxes on the divertor are reduced [22].

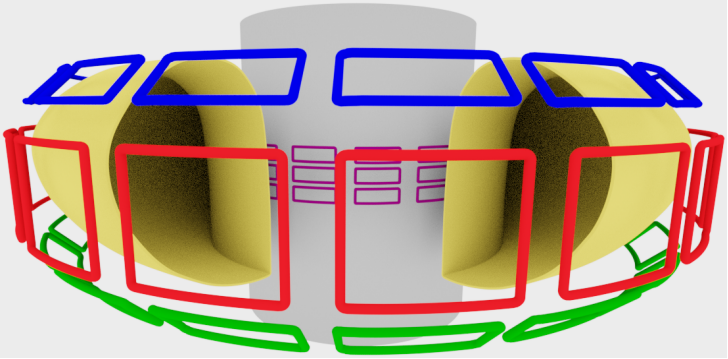

Figure 1.3: Schematic drawing of the RMP coils of TCABR: in red is the middle array of I-coils, while in blue and green is the upper and lower arrays of I-coils, respectively. In magenta, is the array of CP-coils.

Among the techniques to achieve ELM mitigation/suppression, the most promising solution is the application of non-axisymetric, relatively small, RMP fields, which breaks magnetic the field axisymmetry. These fields can create magnetic islands at rational surfaces and, if these islands overlap on the pedestal region, a region of stochastic magnetic field lines is created. This region augments particle and energy radial transport in the plasma edge, reducing edge pressure gradient and parallel current density, which are the drivings for ELMs. The pioneered work on ELM suppression was carried out on the DIII-D tokamak [23], where they achieved ELM-free H-mode plasma operation.

These perturbative fields are produced by RMP coils, which are window frame coils distributed toroidally around the vacuum vessel and can be installed inside or outside of the machine. On TCABR, there will be two groups of RMP coils, where each group composed of 3 sets of 18 RMP coils each. One group is located on the LFS (the I-coils) and another group located on the HFS (the CP-coils), Figure 1.3. Because of the latter set, TCABR will be the first machine to have RMP coils on the HFS and it will be the first machine to generate $n \leq 9$ RMP fields, since each of the six sets is composed of 3 arrays of 18 coils each, *i.e.* a total of 108 RMP coils. Each coil will be independently powered by a power supply on DC mode, with coil currents up to 2 kA, or on AC mode, with coil current up to 1 kA and any waveform up to $f \leq 10$ kHz.

1.5 Outline of this work

In this chapter, an introduction about nuclear fusion, the tokamak device and the problems encountered in H-mode tokamak plasmas was presented. The challenges encountered in developing controlled nuclear fusion were discussed, where the problem of ELMs in H-mode tokamak plasmas and the use of RMP fields to control ELMs were presented.

- Chapter 2 addresses the theory of magnetohydrodynamics (MHD), where the plasma is modelled as a conducting fluid subject to magnetic fields. A simplified model is developed to describe the stability criteria to ELMs in H-mode tokamak plasmas, addressing the main physical topics and details about plasma stability.

- Chapter 3 presents the computational tools used in this thesis, which details about the TCABR H-mode plasma equilibrium calculations are discussed. Lastly, the M3D-C^1 model, a visco-resistive MHD code, and the plasma models used in this thesis are presented.

- Chapter 4 discusses about the stability of the standard H-mode plasma studied for the TCABR. The linear stability of MHD modes is investigated, analysing the nature of unstable modes. Furthermore, a scan of 2 main plasma edge quantities is carried out to evaluate the plasma stability sensitivity.

- In chapter 5, the design of the RMP coils for the TCABR is carried, where the physical criteria used are presented. A coil current and a coil geometry optimisations for the I- and CP-coils are executed in order to reduce the coil current amplitude and satisfy the physical criteria.

- Chapter 6 summarises the main results and conclusions of this work.

Chapter 2

Theoretical background

In this chapter, the theoretical background about ELMs and plasma stability is presented, where a simplified analytic physical model is developed. This model addresses the main topics about ELMs and their criteria.

2.1 The ideal MHD model

Tokamak plasmas can be modelled as visco-resistive conducting fluids subject to strong magnetic fields. Therefore, plasmas can be described through a set of non-linear fluid and electromagnetic equations that form the well known magnetohydrodynamic (MHD) model. When viscosity and resistivity are neglected, the remaining set of equations gives rise to the so-called ideal MHD model [7]:

$$\frac{\partial \rho_m}{\partial t} + \boldsymbol{\nabla} \cdot (\rho_m \, \boldsymbol{u}) = 0 \tag{2.1a}$$

$$\rho_m \left[\frac{\partial}{\partial t} + (\boldsymbol{u} \cdot \boldsymbol{\nabla}) \right] \boldsymbol{u} = \boldsymbol{J} \times \boldsymbol{B} - \boldsymbol{\nabla} p \tag{2.1b}$$

$$\frac{\mathrm{d}}{\mathrm{d}t} \left(\frac{p}{\rho_m^{\gamma}} \right) = 0 \tag{2.1c}$$

$$\boldsymbol{E} + \boldsymbol{u} \times \boldsymbol{B} = 0 \tag{2.1d}$$

$$\boldsymbol{\nabla} \times \boldsymbol{E} = -\frac{\partial \boldsymbol{B}}{\partial t} \tag{2.1e}$$

$$\boldsymbol{\nabla} \times \boldsymbol{B} = \mu_0 \boldsymbol{J} \tag{2.1f}$$

$$\boldsymbol{\nabla} \cdot \boldsymbol{B} = 0 \tag{2.1g}$$

where ρ_m, $\boldsymbol{u}$, p, $\boldsymbol{J}$, $\boldsymbol{B}$, $\boldsymbol{E}$ are plasma mass density, velocity, pressure, current density, magnetic field and electric field.

2.2 Toroidally symmetric ideal MHD equilibria

Using the set of equations 2.1, one can describe the equilibrium of a plasma in a tokamak. Firstly, one can define the flux of the poloidal component of the magnetic field:

$$\psi = \int \boldsymbol{B} \cdot d\boldsymbol{A} \tag{2.2}$$

where the integration is done over a circle located at a distance Z above the origin of a cylindrical coordinate system and centred with the Z-axis. Since the magnetic field is toroidally symmetric, the integral is just:

$$\psi(R, Z) = 2\pi \int_0^R B_z(R', Z)\, R'\, dR' \tag{2.3}$$

Differentiating with respect to R:

$$\frac{\partial \psi}{\partial R} = 2\pi R\, B_Z \implies B_Z(R, Z) = \frac{1}{2\pi R}\frac{\partial \psi}{\partial R} \tag{2.4}$$

Using Ampère's law (Equation 2.1g) and assuming axisymmetry ($\frac{\partial B_\phi}{\partial \phi} = 0$), B_R is:

$$B_R(R, Z) = -\frac{1}{2\pi R}\frac{\partial \psi}{\partial Z} \tag{2.5}$$

These expressions can be combined to provide the vector poloidal magnetic field:

$$\boldsymbol{B}_{\text{pol}} = \frac{\boldsymbol{\nabla}\psi \times \hat{\boldsymbol{\phi}}}{2\pi R} \tag{2.6}$$

where $\hat{\boldsymbol{\phi}}$ is the unitary vector in the toroidal direction. Hence, the magnetic field in a toroidally symmetric system can be written as:

$$\boldsymbol{B} = \frac{\boldsymbol{\nabla}\psi \times \hat{\boldsymbol{\phi}}}{2\pi R} + B_\phi\, \hat{\boldsymbol{\phi}} \tag{2.7}$$

Using Equation (2.1f), the plasma current density can be written as:

$$\boldsymbol{J} = \frac{1}{\mu_0}\left[\frac{\boldsymbol{\nabla}(R\, B_\phi) \times \hat{\boldsymbol{\phi}}}{R} - \frac{\Delta^* \psi}{R}\hat{\boldsymbol{\phi}}\right] \tag{2.8}$$

where Δ^* is $R\frac{\partial}{\partial R}\left(\frac{1}{R}\frac{\partial}{\partial R}\right) + \frac{\partial^2}{\partial Z^2}$.

Considering a stationary equilibrium ($\boldsymbol{u} = 0$), the momentum balance equation (Equation 2.1b) is reduced to:

$$\boldsymbol{J} \times \boldsymbol{B} = \boldsymbol{\nabla} p \tag{2.9}$$

Since $\boldsymbol{J} \cdot \boldsymbol{J} \times \boldsymbol{B} = \boldsymbol{B} \cdot \boldsymbol{J} \times \boldsymbol{B} = 0$, one finds that $\boldsymbol{J} \cdot \boldsymbol{\nabla} p = 0$ and $\boldsymbol{B} \cdot \boldsymbol{\nabla} p = 0$. Therefore, $\boldsymbol{J}$ and $\boldsymbol{B}$ are perpendicular to $\boldsymbol{\nabla} p$. Note that:

$$\boldsymbol{B} \cdot \boldsymbol{\nabla} p = 0 \implies B_\phi \hat{\boldsymbol{\phi}} \cdot \boldsymbol{\nabla} p + \frac{1}{R} \boldsymbol{\nabla} \psi \times \hat{\boldsymbol{\phi}} \cdot \boldsymbol{\nabla} p = 0 \tag{2.10}$$

where the first term is zero because of the toroidal symmetry ($\frac{\partial p}{\partial \phi} = 0$). Since $\boldsymbol{\nabla} \psi \times \hat{\boldsymbol{\phi}} \cdot \boldsymbol{\nabla} p = \hat{\boldsymbol{\phi}} \cdot \boldsymbol{\nabla} \psi \times \boldsymbol{\nabla} p$, therefore:

$$\boldsymbol{B} \cdot \boldsymbol{\nabla} p = 0 \implies \frac{1}{R} \hat{\boldsymbol{\phi}} \cdot \boldsymbol{\nabla} \psi \times \boldsymbol{\nabla} p = 0 \implies \hat{\boldsymbol{\phi}} \cdot \boldsymbol{\nabla} \psi \times \boldsymbol{\nabla} p = 0 \implies p = p(\psi) \tag{2.11}$$

Therefore, $\boldsymbol{\nabla} p$ can be written in terms of ψ: $\boldsymbol{\nabla} p = \frac{\mathrm{d}p}{\mathrm{d}\psi} \boldsymbol{\nabla} \psi$. The same idea used in $\boldsymbol{B} \cdot \boldsymbol{\nabla} p = 0$ can be applied in $\boldsymbol{J} \cdot \boldsymbol{\nabla} p = 0$:

$$\boldsymbol{J} \cdot \boldsymbol{\nabla} p = 0 \implies \boldsymbol{\nabla}(R\, B_\phi) \times \hat{\boldsymbol{\phi}} \cdot \boldsymbol{\nabla} p - \Delta^* \psi \hat{\boldsymbol{\phi}} \cdot \boldsymbol{\nabla} p = 0 \tag{2.12}$$

Since p is toroidally symmetric ($\frac{\partial p}{\partial \phi} = 0$), the second term is zero. The first term can be rewritten as $\boldsymbol{\nabla}(R\, B_\phi) \times \hat{\boldsymbol{\phi}} \cdot \boldsymbol{\nabla} p = \hat{\boldsymbol{\phi}} \cdot \boldsymbol{\nabla} p \times \boldsymbol{\nabla}(R\, B_\phi)$, therefore:

$$\boldsymbol{J} \cdot \boldsymbol{\nabla} p = 0 \implies \hat{\boldsymbol{\phi}} \cdot \boldsymbol{\nabla} p \times \boldsymbol{\nabla}(R\, B_\phi) = 0 \implies R\, B_\phi = F = F(\psi) \tag{2.13}$$

Hence, $\boldsymbol{\nabla} F = \boldsymbol{\nabla}(R\, B_\phi)$ can be described as: $\boldsymbol{\nabla} F = \frac{\mathrm{d}F}{\mathrm{d}\psi} \boldsymbol{\nabla} \psi$. Using the results from Equations (2.12) and (2.13), Equation (2.8) can be rewritten as:

$$\boldsymbol{J} = \frac{1}{\mu_0} \left(\frac{1}{R} \frac{\mathrm{d}F}{\mathrm{d}\psi} \boldsymbol{\nabla} \psi \times \hat{\boldsymbol{\phi}} - \frac{1}{R} \Delta^* \psi\, \hat{\boldsymbol{\phi}} \right) \tag{2.14}$$

Finally, substituting Equations (2.7) and (2.14) on Equation (2.9), one obtains:

$$\Delta^* \psi = -\mu_0\, R^2 \frac{\mathrm{d}p}{\mathrm{d}\psi} - \frac{1}{2} \frac{\mathrm{d}F^2}{\mathrm{d}\psi} \tag{2.15}$$

This equation is known as the Grad-Shafranov (GS) equation [24, 25] and it is a non-linear, elliptic, second order, partial differential equation that, in most cases of interest, must be solved numerically. To solve the GS equation, two free flux functions must be specified: the plasma pressure, $p(\psi)$, and the poloidal current function, $F(\psi)$. In addition, boundary conditions must be specified on the boundary of a closed domain. Several numerical methods exist to solve the GS equation, with the most widely used is the so-called iterative Picard method and various equilibrium codes have been written [26, 27, 28, 29, 30].

2.3 The energy principle of ideal MHD

In future fusion power plants, plasmas will have to be operated within, and relatively far from, the stability boundaries, which are limits in the operational space that determine the regions of stable plasma operation. To find whether an ideal MHD equilibrium is stable or unstable, one can perturb the equilibrium and observe whether the plasma returns to its original configuration (stable equilibrium) or whether the plasma continue evolving further away from the original configuration (unstable equilibrium). Mathematically, this is performed through a linearisation of the ideal MHD equations 2.1 around a particular equilibrium configuration. In this approach, all the variables of the system (n, $\boldsymbol{u}, p$, $\boldsymbol{E}$, $\boldsymbol{B}$, $\boldsymbol{J}$) are Taylor expanded around their respective equilibrium values:

$$f(\boldsymbol{r}, t) = f_0(\boldsymbol{r}) + \epsilon\, f_1(\boldsymbol{r}, t) + \epsilon^2\, f_2(\boldsymbol{r}, t) + \dots \tag{2.16}$$

where ϵ is a control parameter and f_0 can be any variable of the system. The perturbed quantities are also Fourier decomposed:

$$f_1(\boldsymbol{r}, t) = \sum_{j=-\infty}^{\infty} f_1^j(\boldsymbol{r})\, e^{-i\,\omega_j\, t} \tag{2.17}$$

Following the same procedures used in Classical Mechanics, one defines the perturbed plasma velocity $\boldsymbol{u}_1$ as:

$$\boldsymbol{u}_1 = \frac{\mathrm{d}\boldsymbol{\xi}}{\mathrm{d}t} \tag{2.18}$$

where $\boldsymbol{\xi}$ is the plasma displacement. At $t = 0$, the perturbed variables are all set to zero: $\boldsymbol{B}_1(\boldsymbol{r}, t = 0) = \rho_1(\boldsymbol{r}, t = 0) = p_1(\boldsymbol{r}, t = 0) = \boldsymbol{\xi}(\boldsymbol{r}, t = 0) = \boldsymbol{v}_1(\boldsymbol{r}, t = 0) = \boldsymbol{E}_1(\boldsymbol{r}, t = 0) = \boldsymbol{J}_1(\boldsymbol{r}, t = 0) = 0$. This means that at $t = 0$, the plasma is at equilibrium. Following the procedure just described, the first-order mass conservation (Equation 2.1a), adiabatic energy (Equation 2.1c) and momentum (Equation 2.1b) become:

$$\frac{\partial \rho_1}{\partial t} = -\boldsymbol{\nabla} \cdot (\rho_0\, \boldsymbol{v}_1) \implies \rho_1 = -\boldsymbol{\nabla} \cdot (\rho_0\, \boldsymbol{\xi}) \tag{2.19}$$

$$\frac{\partial p_1}{\partial t} = -p_0 \gamma\, \boldsymbol{\nabla} \cdot \boldsymbol{v}_1 - \boldsymbol{v}_1 \cdot \boldsymbol{\nabla} p_0 \implies p_1 = -p_0 \gamma \boldsymbol{\nabla} \cdot \boldsymbol{\xi} - \boldsymbol{\xi} \cdot \boldsymbol{\nabla} p_0 \tag{2.20}$$

$$\rho_0 \frac{\partial \boldsymbol{v}_1}{\partial t} = \boldsymbol{J}_0 \times \boldsymbol{B}_1 + \boldsymbol{J}_1 \times \boldsymbol{B}_0 - \boldsymbol{\nabla} p_1 \tag{2.21}$$

Combining Ohm's Law (Equation 2.1d) and Faraday's Law (Equation 2.1e) yields:

$$\frac{\partial \boldsymbol{B}_1}{\partial t} = \boldsymbol{\nabla} \times (\boldsymbol{v}_1 \times \boldsymbol{B}_0) \implies \boldsymbol{B}_1 = \boldsymbol{\nabla} \times (\boldsymbol{\xi} \times \boldsymbol{B}_0) \tag{2.22}$$

Substituting Equations (2.19) and (2.20) into Equation (2.21):

$$\rho_0 \frac{\partial^2 \boldsymbol{\xi}}{\partial t^2} = \frac{1}{\mu_0}[(\boldsymbol{\nabla} \times \boldsymbol{B}_0) \times \boldsymbol{B}_1 + (\boldsymbol{\nabla} \times \boldsymbol{B}_1) \times \boldsymbol{B}_0] + \boldsymbol{\nabla}(p_0\, \gamma \boldsymbol{\nabla} \cdot \boldsymbol{\xi} + \boldsymbol{\xi} \cdot \boldsymbol{\nabla} p_0) \tag{2.23}$$

where $\boldsymbol{B}_1$ is related to $\boldsymbol{\xi}$ through Equation (2.22). Therefore, Equation (2.23) is only dependent of the equilibrium values of the variables of the system and plasma displacement. A reduced form of this equation is:

$$\rho_0 \frac{\partial^2 \boldsymbol{\xi}}{\partial t^2} = \boldsymbol{F}(\boldsymbol{\xi}) \tag{2.24}$$

which $\boldsymbol{F}(\boldsymbol{\xi})$ is called MHD force operator. Using Fourier decomposition, the partial derivative equation transforms into an eigenvalue/eigenfunction problem:

$$-\omega^2 \, \rho_0 \, \boldsymbol{\xi} = \boldsymbol{F}(\boldsymbol{\xi}) \tag{2.25}$$

where ρ_0 works as a weight function. The force operator $\boldsymbol{F}$ is self-adjoint [31] and, therefore, the eigenvalues ω^2 are real and the correspondent eigenfunctions $\boldsymbol{\xi}_n$ form a set of orthogonal basis functions. Hence, any solution can be written as a sum of the eigenfunctions multiplied by their respective weight. Since eigenvalues ω^2 are real, the stability properties of the system is determined as follows:

- If $\omega^2 > 0$, then ω is real. Therefore, the variables have a bounded oscillatory behaviour around the equilibrium, *i.e.* the system is stable.
- If $\omega^2 < 0$, then ω is imaginary. Hence, there is an exponentially growing solution and an exponentially decaying solution. Since an exponentially growing solution exists, the system is unstable.

Since $\boldsymbol{F}$ is self-adjoint, an energy principle can be formulated based on the Ritz' variational principle [32]. The idea here is to transform the eigenvalue/eigenvector problem into an energy problem (scalar). This can be done by multiplying Equation (2.25) by $\boldsymbol{\xi}^*$ and integrating it over the plasma volume:

$$\frac{\omega^2}{2} \int -\rho_0 \left|\xi\right|^2 dV = \frac{1}{2} \int \boldsymbol{\xi}^* \cdot \boldsymbol{F}(\boldsymbol{\xi}) \, dV = \delta W(\boldsymbol{\xi}^*, \boldsymbol{\xi}) \tag{2.26}$$

Here, the left hand side integral is associated to the plasma kinetic energy of the perturbed system, $K(\boldsymbol{\xi}^*, \boldsymbol{\xi})$, and the right hand side integral corresponds to the work done by the $\boldsymbol{F}$ when each plasma volume element is displaced by ξ. Hence:

$$\omega^2(\boldsymbol{\xi}^*, \boldsymbol{\xi}) = \frac{\delta W(\boldsymbol{\xi}^*, \boldsymbol{\xi})}{K(\boldsymbol{\xi}^*, \boldsymbol{\xi})} \tag{2.27}$$

Since this relation is valid for any $\boldsymbol{\xi}$, ω^2 is no longer an eigenvalue. However, a relation between ω^2 and the eigenvalues of the problem can still be obtained by writing $\boldsymbol{\xi}$ as:

$$\boldsymbol{\xi} = \sum_j a_j \, \boldsymbol{\xi}_j \tag{2.28}$$

where $\boldsymbol{\xi}_j$ is the j-th eigenfunction. Since this problem is linear, one can substitute Equation (2.28) into Equation (2.27), thus yielding:

$$\omega^2 = -\frac{\sum_i \sum_j a_j^* \, a_i \int \boldsymbol{\xi}_i^* \cdot \boldsymbol{F}(\boldsymbol{\xi_j}) \, dV}{\sum_i \sum_j a_j^* \, a_i \int \rho_0 \, \boldsymbol{\xi}_i^* \boldsymbol{\xi}_j \, dV} \tag{2.29}$$

The denominator integral corresponds to an orthogonality relation: $\int \rho_0 \, \boldsymbol{\xi}_i^* \boldsymbol{\xi}_j \, dV = \delta_{ij}$. Using equation (2.25) on the numerator integral yields: $\omega_j^2 \int \rho_0 \, \boldsymbol{\xi}_i^* \boldsymbol{\xi}_j \, dV = \omega_j^2 \delta_{ij}$, in which one has made use of the orthogonality relation. Hence:

$$\omega^2 = \frac{\sum\limits_j |a_j|^2 \omega_j^2}{\sum\limits_j |a_j|^2} \tag{2.30}$$

where ω_j is the j-th eigenvalue. Hence, ω^2 is a weighted sum of the eigenvalues of the system. With this relation, a more deep meaning of ω^2 can be understood:

- When $\omega^2 < 0$, there must be, at least, one negative ω_j^2, therefore the system is unstable;
- When $\omega^2 > 0$, no conclusion can be made, except if one proves $\omega^2 > 0$ for any test plasma displacement. Then, the system is stable.

Since $K(\boldsymbol{\xi}^*, \boldsymbol{\xi})$ is always positive, the sign of ω^2 is determined by $\delta W(\boldsymbol{\xi}^*, \boldsymbol{\xi})$, hence:

- If $\delta W > 0$, the system is stable;
- If $\delta W < 0$, the system is unstable.

The energy principle can be extended if one considers that the plasma is surrounded by a vacuum region, which is then surrounded by a conducting wall. This leads to the so-called extended energy principle. In this principle, the boundary conditions at interface are:

- At any material wall, $\boldsymbol{\xi}_n = 0$. In addition, if an ideally conducting wall is considered, $\boldsymbol{B}_n = 0$ at the ideally conducting wall. All plasma variables, such as ρ_m, $\boldsymbol{u}$ and p, are zero outside the conducting wall;
- At the plasma-vacuum interface, $\boldsymbol{B}_{1,n}$ is continuous, while $\boldsymbol{B}_{1,t}$ might be discontinuous across the interface, which indicates the existence of a surface current density flowing at the interface.

Applying these conditions, a rearrangement of δW can be done, leading to [31]:

$$\delta W = \delta W_F + \delta W_V + \delta W_S \tag{2.31}$$

where δW_F is the fluid (plasma) contribution, δW_V is the vacuum contribution and δW_S is the plasma surface contribution. Each term can be written as [1]:

$$\delta W_F = \frac{1}{2} \int_{\text{Fluid}} \left[\frac{|B_{1,\perp}|^2}{2\,\mu_0} + \frac{B_{0,\perp}^2}{2\,\mu_0} |\boldsymbol{\nabla} \cdot \boldsymbol{\xi}_\perp + 2\boldsymbol{\xi}_\perp \cdot \boldsymbol{\kappa}|^2 + \gamma\, p_0 |\boldsymbol{\nabla} \cdot \boldsymbol{\xi}|^2 - \right.$$
$$\left. - 2(\boldsymbol{\xi}_\perp \cdot \boldsymbol{\nabla} p_0)(\boldsymbol{\kappa} \cdot \boldsymbol{\xi}_\perp^*) - \frac{j_{0,||}}{B_0} (\boldsymbol{\xi}_\perp^* \times \boldsymbol{B_0}) \cdot \boldsymbol{B}_1 \right] dV \tag{2.32}$$

$$\delta W_V = \frac{1}{2} \int_{\text{Vacuum}} \frac{B_1^2}{2\,\mu_0} \, dV \tag{2.33}$$

$$\delta W_S = \frac{1}{2} \int_{\text{Surface}} |\boldsymbol{n} \cdot \boldsymbol{\xi}_\perp|^2 \, \boldsymbol{n} \cdot \left\| \boldsymbol{\nabla} \left(p_0 + \frac{B_0^2}{2\,\mu_0} \right) \right\| dS \tag{2.34}$$

where $\boldsymbol{n}$ is the normal vector of the surface and the double line indicates the discontinuity on the plasma-vacuum interface. By the stability criteria, the vacuum term only contributes to stability, while the surface term depends if the thermal and magnetic pressure and equilibrium magnetic energy gradient jump are parallel or anti-parallel to the normal vector. The fluid term is usually the most important in determining the stability of the system and each term inside its integral correspond to a different plasma behaviour. The first term in the integral represents the amount of energy required to perturb the magnetic field and it is related to the shear Alfvén waves; the second term represents the energy needed to bend the equilibrium magnetic field and to compress the plasma, and it is related to compression Alfvén waves; the third term represents the stored energy of ideal plasma due to an adiabatic compression and it is related to sonic waves. Note that all these three terms are positive, since they are quadratic, which leads to plasma stabilisation. However, the last two terms can be destabilising and plasma stability depends on their signs.

The fourth term of the fluid contribution gives rise to pressure driven instabilities. Its sign will depend on the relative directions of $\boldsymbol{\nabla} p_0$ and magnetic field curvature $\boldsymbol{\kappa}$: if both vectors are parallel, this term is negative, making the plasma more unstable. However, if they are anti-parallel, the term is positive, hence the term is stabilising. In tokamaks, both situations occur: at high field side (HFS), this term is stabilising, while at low field side (LFS), this term is destabilising. Therefore, stability of pressure driven modes depend on the integral of $\boldsymbol{\kappa}$ along the field line: if the contribution from the LFS is larger than that from the HFS, it leads to a unstable mode. Examples of pressure driven instabilities in tokamaks are interchange and ballooning modes.

The fifth term of the fluid contribution gives rise to current driven instabilities, in which current densities parallel to the equilibrium magnetic field may lead to instabilities. Examples of instabilities are kink and peeling modes.

2.4 Extended energy principle for a screw pinch

A circular cross section plasma in a tokamak can be modelled as a periodic screw pinch, *i.e.* all the variables of the system must be periodic in both the poloidal and the toroidal directions. Hence, one can perform a spatial Fourier decomposition of the plasma displacement, where the toroidal mode number n is related to the axial wave vector k_z through $k_z = -n/R_0$, which R_0 is the major radius of an equivalent torus. A important connection between the periodic screw pinch and the tokamak models is that the axial direction of a screw pinch z is related to the toroidal angle through $\phi = z/R_0$. From this point, all toroidal components in a toroidal plasma, *e.g.* B_ϕ, will be related to the axial component (z direction), *i.e.* B_z. Therefore, the Fourier decomposition of the plasma displacement is:

$$\boldsymbol{\xi}(r, \theta, z) = \boldsymbol{\xi}(r)\, e^{i\left(m\theta - \frac{n}{R_0} z\right)} \tag{2.35}$$

Since this is a periodic screw pinch model, $\boldsymbol{\xi}$ can be decomposed as:

$$\boldsymbol{\xi} = \xi_r\, \hat{\boldsymbol{r}} + \xi_\eta\, \hat{\boldsymbol{\eta}} + \xi_{||}\, \hat{\boldsymbol{e}}_{||} \tag{2.36}$$

where $\hat{\boldsymbol{e}}_{||}$ is the direction parallel to the equilibrium magnetic field line and $\hat{\boldsymbol{\eta}}$ is perpendicular to both $\hat{\boldsymbol{r}}$ and $\hat{\boldsymbol{e}}_{||}$. Let us now turn the attention to the stability analysis of the screw pinch. Since compression helps to stabilise the plasma, let us consider instabilities that do not compress the plasma, *i.e.* let us impose that: $\boldsymbol{\nabla}\cdot\boldsymbol{\xi}=0$. With this assumption, one can eliminate from Equation (2.32) its stabilising contribution. Because η is in a flux surface and it appears on the Equation (2.32) through the Fourier decomposition (Equation 2.35), it will only depend on r and η. Therefore, one can minimise Equation (2.32) with respect to η. After some extensive algebra, the Equation can be rewritten as [1]:

$$\delta W = \frac{2\pi^2 R_0}{\mu_0}\int_0^a (f\,\xi_r'^2 + g\,\xi_r^2)\,dr + \left|\frac{2\pi^2 B_z^2}{\mu_0 R_0}\xi_r^2\left[\frac{n^2-\frac{m^2}{q^2}}{\frac{n^2}{R_0^2}+\frac{m^2}{r^2}} + \frac{r^2}{m}\Lambda\left(\frac{m}{q}-n\right)^2\right]\right|_{r=a} \tag{2.37}$$

where a is the plasma minor radius, q is the safety factor for a cylindrical and circular cross section plasma, defined by: $q(r)=\frac{r\,B_z}{R_0\,B_\theta}$. The functions f and g are:

$$f = r\frac{B_z^2}{R_0^2}\frac{\left(\frac{m}{q}-n\right)^2}{\frac{n^2}{R_0^2}+\frac{m^2}{r^2}} \tag{2.38}$$

$$g = \frac{2\mu_0\,p'}{1+\left(\frac{m\,R_0}{nr}\right)^2} + r\,\frac{B_z^2}{R_0^2}\left(\frac{m}{q}-n\right)^2\left(1-\frac{1}{\left(\frac{n\,r}{R_0}\right)^2+m^2}\right) + \frac{2n^2\,B_z^2}{r\,R_0^4}\frac{n^2-\frac{m^2}{q^2}}{\left(\frac{n^2}{R_0^2}+\frac{m^2}{r^2}\right)^2} \tag{2.39}$$

and Λ is the stabilising effect of the conducting wall:

$$\Lambda = -\frac{m\,R_0\,K_a}{n\,a\,K_a'}\frac{1-\frac{K'_{r_{\rm wall}}I_a}{I'_{r_{\rm wall}}K_a}}{1-\frac{K'_{r_{\rm wall}}I'_a}{I'_{r_{\rm wall}}K'_a}} \tag{2.40}$$

with $K_r = K_m(nr/R_0)$ and $I_r = I_r(nr/R_0)$ being the modified Bessel functions of first kind and second kind, respectively, and the prime indicates the radial derivative.

An important point in Equation (2.37) is its dependency upon $\frac{m}{q}-n$. Note that function f and the last 2 terms of the function g depend on $\frac{m}{q}-n$. These three terms are stabilising and they all vanish at $q=m/n$. So, there are special surfaces in the plasma that plays a important role in the stability of tokamak plasmas. These surfaces are called rational or resonant surfaces, since m and n are integers. At these surfaces, a field line closes upon itself after n toroidal turns and m poloidal turns.

2.5 ELMs in the ideal MHD model

Edge localised modes (ELMs)[11] are instabilities caused by the coupling of current driven instabilities (peeling modes) with pressure driven modes (ballooning modes). These modes can be quite violent as they can expel huge amounts of energy and particles to the material

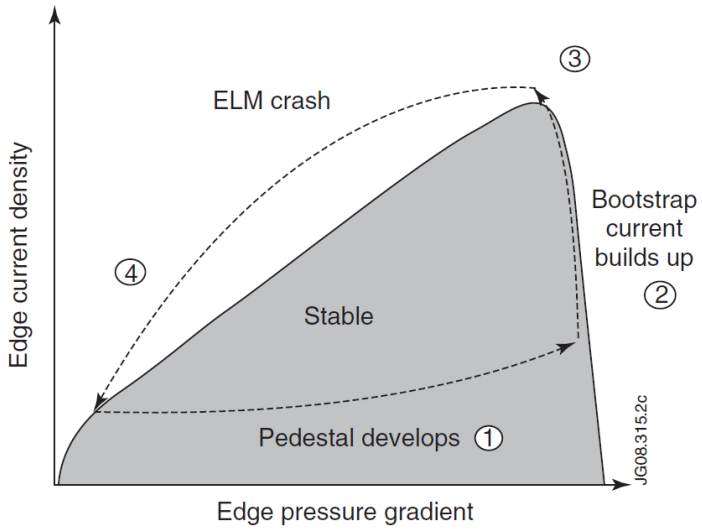

Figure 2.1: A standard ELM cycle: the 1st phase is a linear phase, where edge pressure gradient and parallel edge current density starts to increase; the 2nd phase starts when the edge pedestal pressure is critically stable (ballooning critical) and the edge parallel current density is still building up; in the 3rd phase, the plasma edge is critically stable to ballooning and peeling modes and non-linear processes leads to the ELM crash, ejecting particles and energy to the wall, reducing plasma edge pressure and current density. Reproduced from [1].

walls, causing heat fluxes onto plasma facing components of the order of hundreds of MW/m^2 in large machines such as JET.

These modes are periodic and their periods can be described by a linear phase, in which there is an increase of temperature, pressure, parallel current density in the plasma edge [12, 13, 14, 15] and, consequently, of stored energy, and by non-linear phase, in which the ELM is triggered and particles and energy are expelled from the confined region. A typical ELM cycle is illustrated in Figure 2.1.

Up to this date, there is no unified ELM description, but a phenomenological approach has been used to describe different types of ELMs (Figure 2.2):

- *Type I ELMs*: instabilities in which peeling and ballooning modes are coupled. These modes are the most violent, ejecting large amounts of particles and energy to the wall, above any material heat flux threshold [16]. The toroidal mode number of this instability ranges from $n = 7 - 14$.

- *Type II ELMs*: instabilities mainly triggered by ballooning modes on scenarios with high triangularity (δ), poloidal beta (β_p) and safety factor at flux surface $\psi_N = 0.95$ (q_{95}). These modes are not intense as type I ELMs and, since they are triggered by ballooning modes, the toroidal mode number of this instability is typically high, *i.e.* $n > 15$

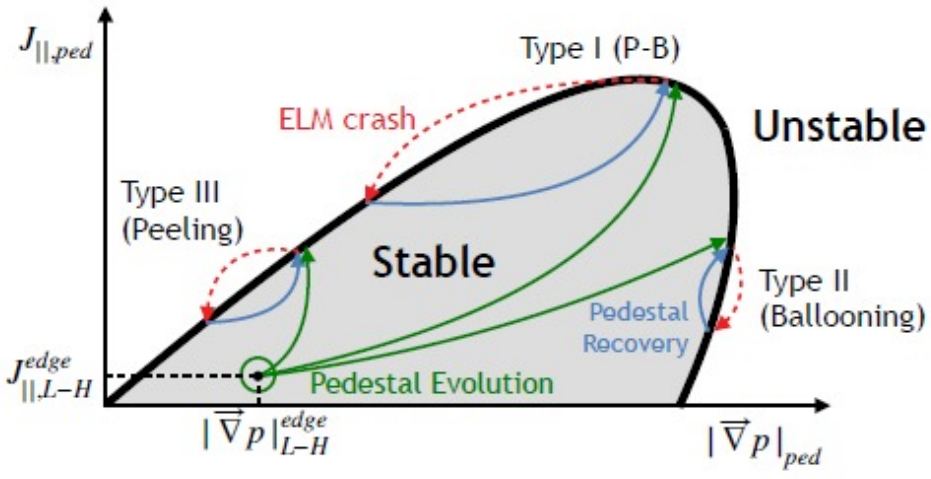

Figure 2.2: A schematic diagram of type I,II and III ELM cycle with its respective characteristics and an example of values of pressure gradient and parallel current in L-H transition

- *Type III ELMs*: instabilities triggered by peeling modes, in which the plasma is stable for pressure gradient modes. This instability is mainly driven by high bootstrap currents and where the plasma scenario is close to L-H threshold transition, with temperature, density and plasma confinement time smaller than the values for a type I ELM scenario.

Applying a minimisation using Euler-Lagrange equation on Equation (2.37) for critically stable to kink modes plasmas, a stability criteria can be derived [1]:

$$\alpha \left[\frac{r}{R_0} \left(1 - \frac{1}{q^2} \right) + s\Delta' - f_t \frac{R_0\, s}{2r} \right] > R_0\, q\, s \left(\frac{j_{||,\mathrm{driven}}}{B} \right) \tag{2.41}$$

where α is the normalised plasma pressure, or ballooning parameter:

$$\alpha = -\frac{2\,\mu_0\, R_0\, q}{B^2} \frac{\mathrm{d}p}{\mathrm{d}r} \tag{2.42}$$

f_t is the trapped particle fraction, s is the magnetic shear

$$s = \frac{r}{q} \frac{\mathrm{d}q}{\mathrm{d}r} \tag{2.43}$$

and Δ' is the radial derivative of the Shafranov shift, defined by:

$$\Delta' = -\frac{r}{R_0} \left(\hat{\beta}_{\mathrm{pol}} + \frac{\hat{\ell}_i}{2} \right) \tag{2.44}$$

Here, $\hat{\beta}_{\mathrm{pol}} = \frac{2\,\mu_0}{B^2_{\mathrm{pol}}} (\langle p \rangle - p)$ is the local poloidal beta and $\hat{\ell}_i = \frac{\langle B^2_{\mathrm{pol}} \rangle}{B^2_{\mathrm{pol}}}$ is the local normalised inductance.

Equation (2.41) is a model which if the inequality is true, the plasma is stable. The first term of the LFS describes the Mercier contribution [1], that can lead to pressure driven modes. The second term of the LFS describes the Pfirsch-Schlüter current, which is an effect of the divergence of the diamagnetic current in a torus that can be not zero in a flux surface. The third term of the left hand side describes the destabilising bootstrap contribution, accounted by the bootstrap current that will be described in the next chapter. The right hand side $j_{||,\text{driven}}$ represents the parallel current with exception of Pfirsch-Schlüter and bootstrap current which are on the left hand side due to their dependence to p'. Since, α is linearly dependent on p', this equation relates $|\boldsymbol{\nabla} p|$ and $J_{||}$ linearly if plasma is critically stable to peeling modes (current driven instabilities). Hence, if the pressure gradient is increased, more parallel current can be induced and the plasma is still stable. However, this equation is only valid when the pressure gradient in the edge is not close to the instability region. When this happens, ballooning theory must be accounted and the relation between parallel density current and pressure gradient is complex, hence, stability studies demand numerical calculations [33, 14].

Chapter 3

Computational tools

This chapter presents the computational tools used in this work. In particular, a detailed description is given to the Plasma Scenario Design (PSD) code, written by Prof. Gustavo Canal, used to generate the TCABR plasma scenarios used in this work.

3.1 The Plasma Scenario Design code

In this section, the main steps followed by the PSD code are described in details. The PSD code not only solves the GS equation for a prescribed plasma boundary, plasma current, etc., but also allows for (*i*) the inclusion of neoclassical effects to the equilibrium, such as the bootstrap current and neoclassical plasma rotation, (*ii*) the automatic adjustment of kinetic profiles when ballooning stability is reached, (*iii*) the calculation of the poloidal field coil currents needed to create the desired equilibrium, among other options.

3.1.1 The TCABR pedestal structure

The characteristics of the H-mode edge pedestal are crucial for characterising the confinement of the core plasma. In addition, understanding and predicting the pedestal pressure and width is essential for characterising the stability of tokamak plasmas. The pedestal is characterised by a steep pressure in the plasma edge (last $5 - 10\,\%$ of the plasma poloidal flux). During the evolution of the properties of the pedestal, the pedestal height (plasma pressure at the pedestal top) increases due to the improvement in confinement, causing a further increase of the pedestal height and pressure gradient, which triggers local pressure driven instabilities that increase the pedestal width. The pedestal height and width continue to grow, but at different rates, such that the edge pressure gradient keeps increasing until a more severe (global MHD) instability is driven, causing the edge pedestal to collapse - the ELM crash. The two instabilities just mentioned are [34]:

- Local kinetic ballooning modes (KBM): a short wavelength instabilities driven by local pressure gradients and kinetic effects [34]. The evolution of the structure of a pedestal limited by KBMs can be calculated using the so-called ballooning critical pedestal (BCP) method, in which the pedestal profile (height and width) is ballooning critical if the centre of the pedestal, *i.e.* where the pressure gradient is

$B\,(T)$	Δ_{ψ_N}	$p_{ped}\,(kPa)$
0.13	0.0592	4.08
0.14	0.0526	3.73
0.15	0.0471	3.44
0.16	0.0425	3.18

Table 3.1: KBM-PBM stability limit in terms of poloidal field.

maximum, is marginally stable (at the ballooning stability threshold) or unstable. Using this method, one can relate the pedestal width (Δ_{ψ_N}) with the local poloidal beta at the pedestal top, $\beta_{p,\mathrm{ped}}$ [34]:

$$\Delta_{\psi_N} = C\sqrt{\beta_{p,\mathrm{ped}}} \implies p_{\mathrm{KBM}} = \frac{1}{2\,\mu_0}\left(\frac{B_{\mathrm{pol}}\,\Delta_{\psi_N}}{C}\right)^2 \tag{3.1}$$

with C depending on ion collisionality and aspect ratio. Studies show that C can assume values between $0.06 - 0.09$. Here, $C = 0.076$ is the used value, which is a value that has been validated in several experiments on DIII-D and is also the value assumed in the EPED code used to predict the pedestal structure of ITER H-mode plasmas. [34].

- Global peeling-ballooning modes (PBMs): coupling of two types of ideal MHD modes: peeling modes, which are current driven, and ballooning modes, which are pressure gradient driven. This coupling generates modes on the pedestal and it has typically an intermediate toroidal mode number ($n = 7 - 14$). The crash of these modes releases particles and energy from the edge pedestal structure, decreasing the pedestal pressure height and gradient. For standard aspect ratio, such as TCABR and DIII-D, the PBM stability boundary can be estimated through a scaling law: [34]:

$$p_{\mathrm{PBM}} = A\,\Delta_{\psi_N}^{3/4} \tag{3.2}$$

with $A = 34\,\mathrm{kPa}$ and Δ_{ψ_N} being the pedestal width in units of normalised poloidal flux.

The pedestal height and width are defined when the pedestal is marginally stable for both KBMs and PBMs modes, Figure 3.1. For TCABR, the poloidal field is in the range of $0.13 - 0.17\,\mathrm{T}$ and the pedestal height and width for each value of poloidal magnetic field can been seen in Figure 3.1. The KBM and PBM marginally stable values for pedestal height and width are given in Table 3.1.

A systematic way of determining the pedestal pressure is through the pedestal electron temperature ($T_{\mathrm{e,ped}}$), which can be estimated through [35]:

$$T_{\mathrm{e,ped}} = 0.034\left(\frac{B_0}{q_{95}}\right)^4\left[\frac{a(1+\kappa_{95})}{I_p}\right]^2\left(\frac{\alpha_c^2}{\bar{n}_e}\right) \tag{3.3}$$

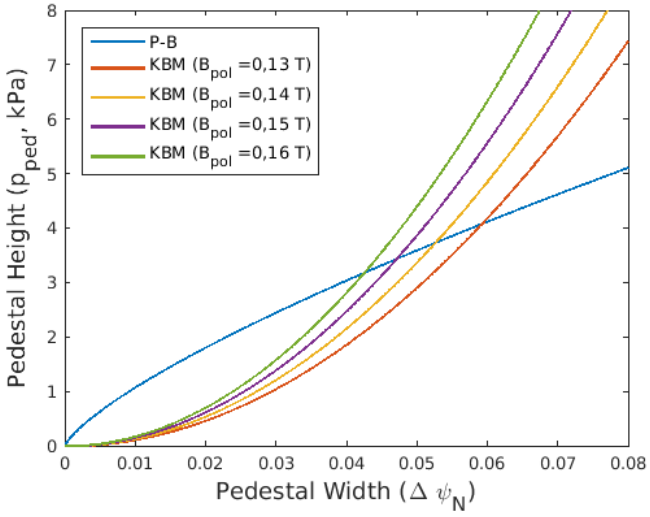

Figure 3.1: Pedestal height and width marginally stable for KBM and PBMs.

where α_c is the critical ballooning parameter, given by:

$$\alpha_c = 0.4\,\hat{s}\left[1 + \kappa_{95}^2(1 + 5\delta_{95}^2)\right] \tag{3.4}$$

Here: $B_0(T)$, q_{95}, $a(m)$, κ_{95}, δ_{95}, $I_p(MA)$, $\bar{n_e}(10^{20})$ and $\hat{s}$ are, respectively, toroidal magnetic field measured at R_0, edge safety factor, plasma minor radius, elongation, triangularity, plasma current, line-averaged electron plasma density and magnetic shear. On the other hand, the pedestal width can be calculated via [33]:

$$\Delta_{\psi_N} = 0.076\,\sqrt{\beta_{p,\mathrm{ped}}} \tag{3.5}$$

which $\beta_{\mathrm{p,ped}}$ is the pedestal poloidal beta, defined by:

$$\beta_{\mathrm{p,ped}} = \frac{4\mu_0\, n_{\mathrm{e,ped}}\, k_B\, T_{\mathrm{e,ped}}}{\langle B_{\mathrm{pol}}\rangle^2} \tag{3.6}$$

where k_B is the Boltzmann constant, $n_{\mathrm{e,ped}}$ and $T_{e,ped}$ are electron pedestal density and temperature, respectively, and $\langle B_{\mathrm{pol}}\rangle$ is the mean value of the poloidal field in the pedestal.

3.1.2 Plasma kinetic profiles

The signature of H-mode tokamak plasmas is the structure of electron temperature, density and, consequently, pressure profiles. These profiles have a pedestal structure in the plasma edge, where they can be modelled as [36]:

$$f(\psi) = f_a + (f_{\mathrm{ped}} - f_a)\tanh\left[\lambda\frac{\psi_a - \psi}{\psi_a - \psi_0}\right] + (f_0 - f_{\mathrm{ped}})\left(\frac{\psi_a - \psi}{\psi_a - \psi_0}\right)^{\mu} \tag{3.7}$$

Here, f represents either temperature or density as a function of the poloidal magnetic flux ψ. f_a is the value in the plasma edge, f_0 is the value at the magnetic axis and f_{ped}

is the value on the pedestal top. λ and μ are free parameters, where the first adjusts the pedestal width and the latter adjusts how the profile peaks at the magnetic axis. With the temperature and density profiles, one can calculate the pressure profile for each specie via:

$$p_\alpha(\text{kPa}) = 16.02\, n_\alpha(10^{20})\, T_\alpha(\text{keV}) \tag{3.8}$$

where the specie pressure is in units of kPa, the specie temperature is in units of keV, the specie density is in units of 10^{20}. Therefore, the total pressure is the sum of the pressure of all species. For the TCABR:

$$p_{\text{tot}} = p_e + p_i + p_C + p_{\text{Fe}} \tag{3.9}$$

where p_e is the electron pressure, p_i is the ion pressure, p_C is the carbon impurity pressure and p_{Fe} is the iron impurity pressure.

In this work, the poloidal plasma rotation is assumed to be purely neoclassical [37]. If one takes equilibrium flux-surface averaged parallel component of the momentum force balance for the main ion and a impurity species, it results in:

$$\langle \boldsymbol{B} \cdot \boldsymbol{\nabla} \cdot \boldsymbol{\Pi}_\alpha \rangle = \langle \boldsymbol{B} \cdot \boldsymbol{F}_\alpha \rangle \tag{3.10}$$

where $\boldsymbol{\Pi}_\alpha$ is the stress tensor and $\boldsymbol{F}_\alpha$ is the source of momentum due to momentum exchange between different fluids. This equation shows the balance between momentum source and viscous forces. When the plasma is in the Pfirsch-Schlüter regime, the ion and impurity poloidal rotation velocities can be derived from equation (3.10) and can be found at [37]. The expressions are the following:

$$v_{\theta,i}^{\text{neo}} = \frac{1}{2} v_{\text{th},i} \rho_i \left(K_1 \frac{1}{L_{T_i}} \right) \frac{B\, B_\phi}{\langle B^2 \rangle} = \frac{1}{2e} F(\psi)\, k(\psi) \frac{\partial T}{\partial \psi} B_\theta \tag{3.11}$$

$$v_{\theta,\alpha}^{\text{neo}} = \frac{1}{2} v_{\text{th},i} \rho_i \left[\left(K_1 + \frac{3K_2}{2} \right) \frac{1}{L_{T_i}} - \frac{1}{L_{p_i}} + \frac{Z_i}{Z_\alpha} \frac{T_\alpha}{T_i} \frac{1}{L_{p_\alpha}} \right] \frac{B\, B_\phi}{\langle B^2 \rangle} \tag{3.12}$$

where $v_{\text{th},i}$ is the ion thermal velocity, ρ_i is the ion Larmor radius, K_1 and K_2 are the collisionality-dependent viscosity coefficients as defined in [37], $F(\psi) = R\, B_\phi$ and $k(\psi)$ are flux-dependent functions, L_{T_i} is the ion temperature gradient scale length, defined as $\frac{1}{L_{T_i}} = \frac{\mathrm{d} \ln T_i}{\mathrm{d}r}$, and L_{p_i} is the ion pressure gradient scale length. It is important to note the strong relation between the ion poloidal rotation velocity and the ion temperature gradient. For the impurity poloidal rotation velocity, there are more intricate relations and both ion temperature and pressure gradient scale lengths are important in the calculations, making impurity poloidal velocity dependent of ion quantities. It is worth noting how small is the contribution of impurity pressure gradient scale length due to the factor $\frac{Z_i}{Z_\alpha}$. In H-mode plasma edge, the impurity poloidal velocity can be large due to the steep ion pressure gradient and impurities rotates typically at the diamagnetic drift direction. On the other hand, the ion poloidal rotation velocity can be zero or even change sign in the pedestal region, as it depends on ion parameters in the plasma edge. The main responsible parameter for this change is the ion collisionality $\nu_{*,i}$, which is closely related to the coefficient K_1.

The ion toroidal velocity on the pedestal top is calculated via neoclassical theory [38]:

$$v_{\phi,\text{ped}} = 0.104 \left(\frac{d_c}{2} - \bar{R}_x \right) \frac{q_{95}\, T_i}{L_\phi\, B_0} \tag{3.13}$$

where $v_{\phi,\text{ped}}$ is in units of km/s, d_c is the poloidal variation of the turbulent plasma viscosity, q_a is the plasma safety factor at $\psi_N = 0.95$, L_ϕ is the e-folding decay length of the plasma potential fluctuation intensity $\left\langle \tilde{\phi}^2 \right\rangle^{1/2}$ in units of cm, T_i is the pedestal top ion temperature in eV and $\bar{R}_x$ is the normalised X-point major radius, defined as:

$$\bar{R}_x = \frac{2\, R_x - (R_\text{out} + R_\text{in})}{(R_\text{out} - R_\text{in})} \tag{3.14}$$

where R_x is the X-point radius, R_out is the major radius of the outer separatrix at the midplane and R_in is the major radius of the inner separatrix at the midplane.

At the magnetic axis, the H-mode plasma toroidal velocity is modelled as [39]:

$$(v_{\phi,\text{axis}})_H = A\, \frac{W_p}{I_p} + (v_{\phi,\text{axis}})_L \tag{3.15}$$

where A is a constant, W_p is the plasma stored energy and $(v_{\phi,\text{axis}})_L$ is the L-mode plasma toroidal velocity at the magnetic axis. For the TCABR, it was observed that the L-mode plasma toroidal velocity at the magnetic axis is 30 km/s.

3.1.3 Inclusion of the bootstrap current

In order to calculate the plasma kinetic equilibrium accurately, one must account for all currents present in the plasma. Due to the non-uniform toroidal magnetic field on a flux surface and low collisionality, electron and ion execute the so-called banana orbits that gives rise to a parallel current density termed bootstrap current. This current is also related to pressure, electron and ion temperature gradients, trapped particle fraction and collisionality [40]:

$$j_{BS} = j_p + J_{Te} + j_{Ti} = -R_0\, p_e\, (g_p + g_{Te} + g_{Ti}) \tag{3.16}$$

where:

$$g_p = L_{31} \frac{1}{p_e} \frac{\partial p}{\partial \psi}, \quad g_{Te} = L_{32}\, \frac{1}{T_e} \frac{\partial T_e}{\partial \psi}, \quad g_{T_i} = L_{34}\, \alpha\, \frac{1 - \frac{p_e}{p}}{\frac{p_e}{p}}\, \frac{1}{T_i} \frac{\partial T_i}{\partial \psi} \tag{3.17}$$

Here, p is the total thermal pressure, p_e is the electron pressure, T_e and T_i are the electron and ion temperatures, while the coefficients L_{31}, L_{32}, L_{34} and α are functions of the electron and ion collisionalities ν_e^*, ν_i^* and the trapped particle fraction f_t.

3.1.4 Power balance

One of the main plasma equations, the power balance accounts all plasma powers due to phenomena such as: radial transport, radiation (line radiation, cyclotron emission and bremsstrahlung) and ohmic heating:

$$\frac{\partial W}{\partial t} = P_{\text{ohm}} + P_{\text{aux}} + P_{\alpha} - P_{\text{rad}} - \frac{W}{\tau_e} \tag{3.18}$$

which W is the total plasma stored thermal energy, P_{ohm} is the ohmic heating power, P_{aux} is the auxiliary power input into the plasma by external methods such as neutral beam injection and microwave heating, P_{α} is the heating power due to fusion-born α-particles, P_{rad} is the power lost due to radiation (line radiation, cyclotron emission and bremsstrahlung) and τ_e is the energy confinement time, which is expressed by a empirical scaling law[41]:

$$\tau_e = 0.0562\, I_p^{0.93}\, B_0^{0.15}\, P_{\text{in}}^{-0.69}\, \bar{n}_e^{0.41}\, M^{0.19}\, R_0^{1.97}\, \kappa^{0.78}\, \epsilon^{0.58} \tag{3.19}$$

where $I_p\,(MA)$ is the plasma current, $B_0\,(T)$ is the toroidal magnetic field measured at R_0, $P_{\text{in}}\,(MW) = P_{\text{ohm}} + P_{\text{aux}} + P_{\alpha}$ is the input power, $\bar{n}_e\,(10^{19})$ is the line-averaged electronic density, M (u.a.) is the isotopic hydrogen mass, $R_0\,(m)$ is the machine major radius, κ is the plasma elongation and $\epsilon = a/R_0$ is the plasma aspect ratio.

In TCABR, there are no auxiliary heating nor fusion power, so $P_{\text{in}} = P_{\text{ohm}}$ and the power balance reduces to:

$$\frac{\partial W}{\partial t} = P_{\text{ohm}} - P_{\text{rad}} - \frac{W}{\tau_e} \tag{3.20}$$

With the ohmic power calculated by:

$$P_{\text{ohm}} = \int \boldsymbol{j} \cdot \boldsymbol{E}\, dV \tag{3.21}$$

Since the externally applied, induced electric field in the plasma is in the toroidal direction and it can be described by a loop voltage V_l: $V_l = \frac{\partial \psi}{\partial t}$, *i.e.* $E_{||} = \frac{V_l}{2\pi R_0}$, one obtains:

$$P_{\text{ohm}} = \int \frac{j_{\text{tor}}\, V_l}{2\pi\, R_0}\, dV \tag{3.22}$$

Radiated power is the sum of line radiation, cyclotron emission and bremsstrahlung power. The first is [6]:

$$P_R = \sum n_e\, n_Z\, R_Z(T_e) \tag{3.23}$$

where n_e is the electron density, n_Z is the impurity density and $R_Z(T_e)$ is the radiated power function, *i.e.* Figure 3.2. The sum accounts all impurities species in the plasma.

For bremsstrahlung, the radiated power is [6]:

$$P_{\text{brem}} = 1.6918 \times 10^{-38}\, Z_{\text{eff}}^2\, n_e\, n_z\, T_e^{1/2} \tag{3.24}$$

where Z_{eff} is the effective ion charge of the impurity. For TCABR, the accounted impurities are iron (Fe), where the iron density is accounted to be about 5×10^{-4} of n_i, and carbon (C), where the carbon density is accounted to be about 3×10^{-2} of n_e.

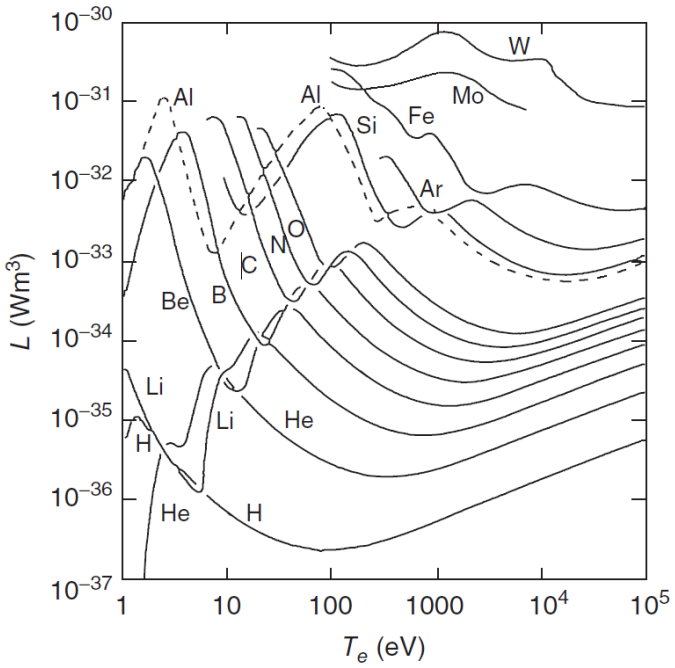

Figure 3.2: Radiated power density normalised to the product of electron and impurity density for several elements. Reproduced from [1].

For the cyclotron radiation, the radiated power density is given by [6]:

$$P_c = \left(\frac{e^4}{3\pi\, \epsilon_0\, m_e^3\, c^3} \right) B^2\, n_e\, T_e \tag{3.25}$$

where ϵ_0 is the vacuum permittivity, m_e is the electron mass and c is the speed of the light in vacuum.

The total plasma stored energy W is calculated via the integral of total pressure:

$$W = \frac{3}{2} \int p_{\text{tot}}\, dV \tag{3.26}$$

3.1.5 H-mode transition and pedestal structure

In 1982, Fritz Wagner and his team at the ASDEX Tokamak in Germany [42], discovered a spontaneous transition in plasma confinement which created a strong gradient on the electron temperature and density and, consequently, electron pressure profiles in the plasma edge. This strong pressure gradient in the plasma edge was associated to a strong reduction in radial transport and a significant improvement in both particle and energy confinement. This new plasma mode of operation is called high confinement mode or simply H-mode, Figure 3.3.

The access to H-mode is not fully understood. Many studies were conducted on a broad range of tokamak sizes, observing how certain parameters influences the H-mode transition:

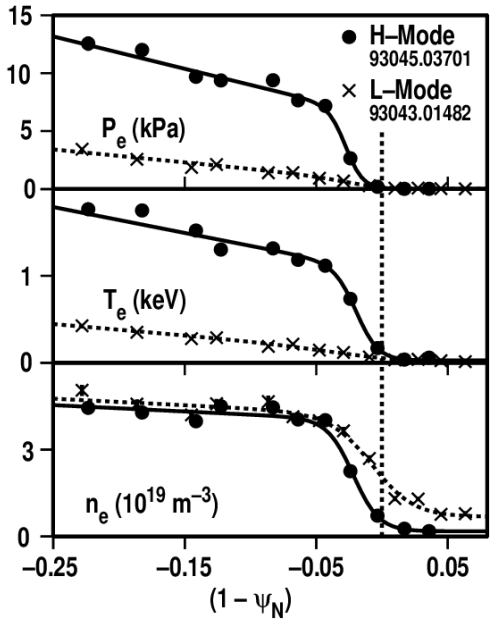

Figure 3.3: Examples of L- and H-mode electron pressure, temperature and density radial profiles for two discharges in DIII-D tokamak. Reproduced from [2].

- Direction of ∇B drift: in JET [43] and DIII-D [44], both teams observed a correlation of the L-H transition with the direction of the ion ∇B drift. In both machines, if the ion ∇B drift points towards the X-point, the transition occurs at a lower power threshold;
- Neutral gas injection: in TCV [45], COMPASS and MAST [46], injection of neutral gas on the HFS allowed H-mode transition to occur at lower power threshold in comparison to injecting neutral gas from the LFS.
- Plasma configuration: in TCV [47], NSTX [48] and MAST [46], the plasma configuration was observed to influence strongly the H-mode access, with diverted configurations reducing the power needed for the transition. In these machines, increasing lower triangularity reduces the L-H power for edge densities above $1.7 \times 10^{19}\, m^{-3}$. In MAST, double-null configurations reduced largely the threshold power, while in NSTX, single-null were preferable.

Using data from 13 machines, a scaling law for the L-H transition was derived in order to estimate the minimum power [49]:

$$P_{\mathrm{LH}}\,(MW) = 0.072\, n_{20}^{0.7}\, B_0^{0.7}\, S^{0.9} \left(\frac{Z_{\mathrm{eff}}}{2}\right)^{0.7} F(A)^{0.5} \tag{3.27}$$

Here $F(A) = 0.1\frac{A}{f(A)}$ with $f(A) = 1 - \sqrt{\frac{2}{1+A}}$, with $A = R_0/a$ being the aspect ratio, n_{20} being the electron density in units of 10^{20} and S is the surface area of plasma boundary. For a TCABR single-null divertor configuration, the L-H power threshold is expected to be about 240 kW.

3.2 The M3D-C^1 model

In this work, the plasma response to RMP fields and the growth rates of MHD instabilities were calculated using the two-fluid visco-resistive MHD code M3D-C^1 [50, 51], which was developed at the Princeton Plasma Physics Laboratory (PPPL). The code was brought to Brazil through a collaboration between PPPL and the TCABR team and the code is installed at the supercomputer Santos Dumont, operated by the National Laboratory of Scientific Computing (LNCC) at Petrópolis - RJ. This code solves the MHD equations on a extended region that includes the confined plasma, scrape-off layer, conducting wall and the vacuum region surrounding the conducting wall. The codes solves the following set of MHD equations through a finite element method, which ensures the continuous property of the value and the derivative of the fields calculated.

$$\frac{\partial n}{\partial t} + \nabla \cdot (n\boldsymbol{u}) = 0, \tag{3.28a}$$

$$nm_i \left(\frac{\partial \boldsymbol{u}}{\partial t} + \boldsymbol{u} \cdot \nabla \boldsymbol{u} \right) = \boldsymbol{J} \times \boldsymbol{B} - \nabla p - \nabla \cdot \boldsymbol{\Pi} + \boldsymbol{F}, \tag{3.28b}$$

$$\begin{aligned} \frac{\partial p}{\partial t} + \boldsymbol{u} \cdot \nabla p + \Gamma p \nabla \cdot \boldsymbol{u} = (\Gamma - 1) \left[Q - \nabla \cdot \boldsymbol{q} + \eta J^2 - \boldsymbol{u} \cdot \boldsymbol{F} - \boldsymbol{\Pi} : \nabla u \right] \\ + \frac{1}{ne} \boldsymbol{J} \cdot \left(\frac{\nabla n}{n} p_e - \nabla p_e \right) + (\Gamma - 1) \boldsymbol{\Pi_e} : \nabla \left(\frac{1}{ne} \boldsymbol{J} \right) \end{aligned} \tag{3.28c}$$

$$\begin{aligned} \frac{\partial p_e}{\partial t} + \boldsymbol{u} \cdot \nabla p_e + \Gamma p_e \nabla \cdot \boldsymbol{u} = (\Gamma - 1) \left[Q_e - \boldsymbol{\nabla \cdot q_e} + \eta J^2 - \boldsymbol{u} \cdot \boldsymbol{F}_e - \boldsymbol{\Pi_e} : \nabla u \right] \\ + \frac{1}{ne} \boldsymbol{J} \cdot \left(\frac{\nabla n}{n} p_e - \nabla p_e \right) + (\Gamma - 1) \left[\boldsymbol{\Pi_e} : \nabla \left(\frac{1}{ne} \boldsymbol{J} \right) + \frac{1}{ne} \boldsymbol{J} \cdot \boldsymbol{F}_e \right] \end{aligned} \tag{3.28d}$$

$$\boldsymbol{\nabla} \times \boldsymbol{E} = -\frac{\partial \boldsymbol{B}}{\partial t}, \tag{3.28e}$$

$$\boldsymbol{\nabla} \times \boldsymbol{B} = \mu_0 \boldsymbol{J}, \tag{3.28f}$$

$$\boldsymbol{E} + \boldsymbol{u} \times \boldsymbol{B} = \eta \boldsymbol{J} + \frac{1}{ne} \left(\boldsymbol{J} \times \boldsymbol{B} - \boldsymbol{\nabla} p_{\mathrm{e}} - \boldsymbol{\nabla \cdot \Pi_e} \right). \tag{3.28g}$$

Here, p is total pressure, $\boldsymbol{u}$ is the fluid velocity, p_e and p are the electron and total plasma pressures, $\boldsymbol{J}$ is the plasma current density, n is the plasma density, $\boldsymbol{E}$ and $\boldsymbol{B}$ are the electric and magnetic fields, m_{i} is the ion mass, Γ is the heat capacity ratio, η is the Spitzer resistivity, $\boldsymbol{\Pi_e}$ and $\boldsymbol{\Pi}$ are the electron and total stress tensors, $\boldsymbol{q_e}$ and $\boldsymbol{q}$ are the electron and total heat flux, Q_e and Q are electron and total external heat, $\boldsymbol{F}_e$ and $\boldsymbol{F}$ are external force acting on the electrons and on the plasma (electrons + ions). This set of equations is solved on an unstructured mesh, generated by a code developed by the

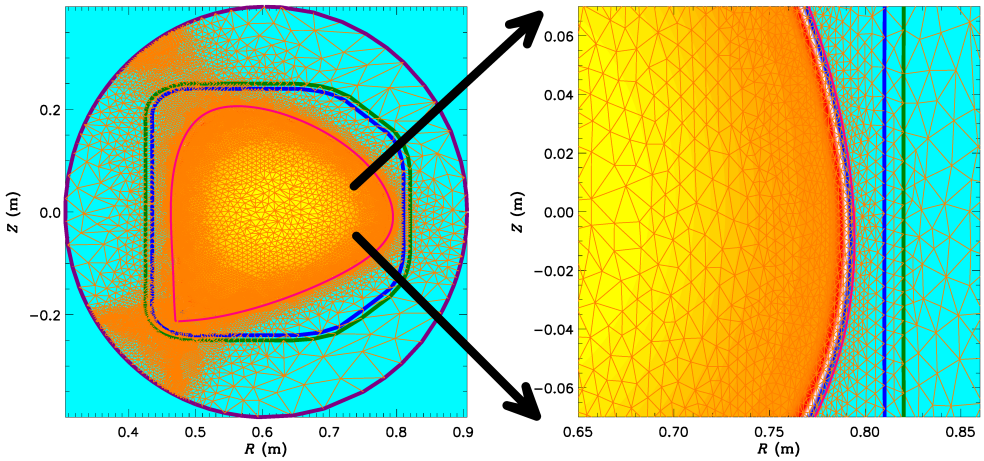

Figure 3.4: The generated mesh used for the M3D-C^1 studies. It has 25957 elements, covering all 3 regions (plasma core, scrape-off layer and vacuum).

private company Simmetrix. Since the main objective is the study of this work is to study the impact of RMP fields on the plasma, the generated mesh has a higher resolution in the plasma edge and around the separatrix for more accurate results, Figure 3.4.

The simulations carried in this work were run on the linear version of the code, where Equations (3.28) are linearised around the equilibrium. This linearised system is then solved on 2 plasma models:

- *Vacuum model* - the RMP field is superposed with the axisymetric equilibrium magnetic field, *i.e.* the plasma does not respond to the externally applied RMP field.
- *Single-fluid model* - the plasma is modelled as single-fluid, which can respond to the externally applied RMP fields.

Chapter 4

Equilibrium and stability of the TCABR standard scenario

Before designing the innovative set of RMP coils for TCABR, it is crucial to construct an accurate MHD equilibria and characterise the stability of the synthetic MHD equilibria generated. These equilibria will be used for designing the RMP coils and, therefore, it is important to estimate how stable/unstable these plasmas are. Since RMP coils are used to control ELMs, some H-mode scenarios must be unstable to MHD modes (peeling-ballooning modes) in order to generate ELMs. The stability of MHD mode is characterised by the growth rate $\gamma = \frac{1}{2}\frac{\mathrm{d}}{\mathrm{d}t}\ln K$, where K is the plasma kinetic energy. A positive growth rate leads to a unstable MHD mode, while a negative growth rate to a stable MHD mode.

This chapter is divided in three pieces: the first part describes the construct of the standard MHD equilibrium scenario used to design the RMP coils; in the second part, an investigation on what MHD modes are unstable in the standard H-mode scenario of TCABR and what is the role of resistivity in their stability; in the final part, one investigates the role of the pedestal structure, as electron temperature at the pedestal top, $T_{\mathrm{e,ped}}$, and electron pedestal width Δ_{ψ_N}, on the stability and examine how sensitive the plasma stability is to these quantities.

4.1 The TCABR H-mode standard scenario

The starting point of any detailed study on plasma stability and plasma response to RMP fields is the ability to create accurate MHD equilibria. In this work, the plasma scenarios used on stability and plasma response studies were constructed using a code developed by Prof. Gustavo Canal (see Section 3.1). It solves the Grad-Shafranov equation for a prescribed plasma shape and position and some important plasma quantities: upper and lower triangularity (δ_u, δ_l), elongation (κ), toroidal magnetic field at the magnetic axis (B_0), plasma current (I_p), ion and electron temperatures and densities at R_0 ($T_{\mathrm{i,0}}$, $T_{\mathrm{e,0}}$, $n_{\mathrm{i,0}}$, $n_{\mathrm{e,0}}$), electron and ion density at R_0 ($n_{\mathrm{i,ped}}$, $n_{\mathrm{e,ped}}$) and effective ion charge (Z_{eff}). With these quantities, the code simulates the temperature, density, pressure, current and rotation profiles, also calculating dynamic quantities such as collisionality, bootstrap current and plasma poloidal and toroidal rotation velocities. According to

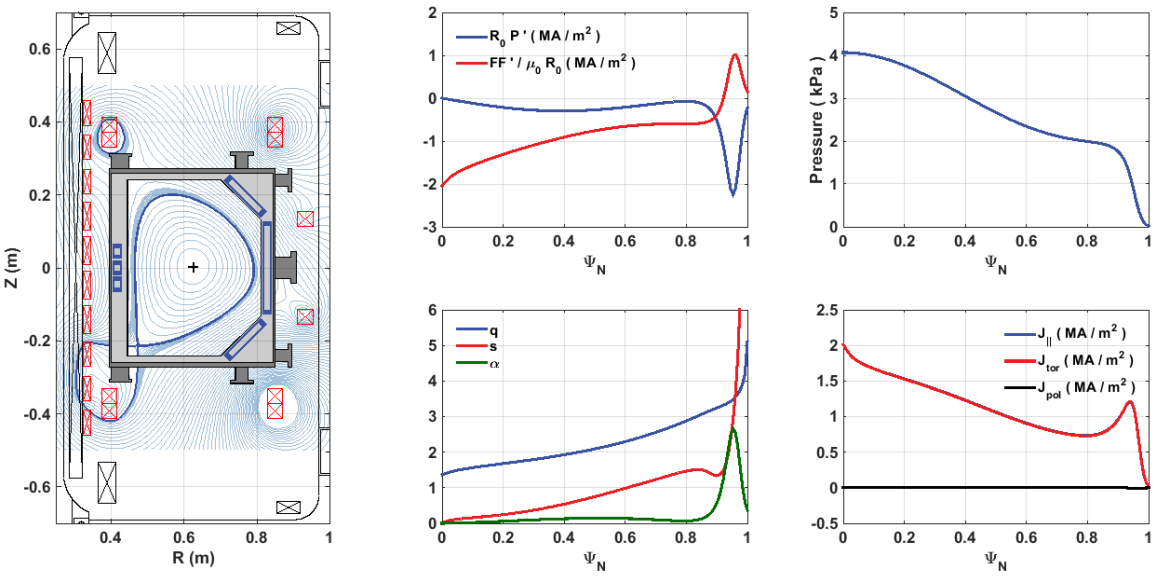

Figure 4.1: Equilibrium profiles of the standard scenario. In this scenario, the main plasma parameters are: $\mathrm{I_p} = 107\,\mathrm{kA}$, $B_0 = 1.2\,\mathrm{T}$, $q_{95} = 3.5$, $\kappa = 1.27$, $\delta_u = 0.4$, $\delta_l = 1.0$, $\psi_{\mathrm{N,ped}} = 0.92$.

the prescribed plasma shape, the code tries to shape the plasma by applying current on poloidal field (PF) coils. The code also accounts for the mutual coupling among the ohmic coil, PF coils, the vacuum vessel and the plasma. The code converges when the error between 2 consecutive interactions is smaller than a prescribed value. Since we are interested in the pedestal studies, a script to simulate the pedestal structure was also included in the code. For the RMP studies, a standard H-mode scenario was generated where the equilibrium and kinetic quantities are calculated and shown in Figures 4.1 and 4.2.

4.2 Linear stability against edge localised modes

The first issue to be addressed in the standard H-mode scenario in TCABR is whether the plasma is unstable to any MHD mode that can lead to an ELM. To address this issue, stability calculations using the M3D-C^1 were ran for the standard H-mode scenario and the growth rate (γ) of the MHD modes were analysed for various toroidal mode number, $n_{\mathrm{tor}} = 1$ to 12, Figure 4.3. The code evolves the MHD equations (3.28) for about 150 τ_A, where $\tau_A = \frac{a}{v_A}$ is a constant Alfvén time, related to the plasma minor radius and the Alfvén velocity $v_A = \frac{B}{\sqrt{\mu_0\,\rho_m}}$, with $B = 1\,T$ and $\rho_m = m_i\,n_0$ is the plasma mass density with $n_0 = 10^{20}\,m^{-3}$.

The simulations, the growth rates γ calculated by the M3D-C^1 code are then normalised by the effective ion diamagnetic frequency, ω_i^*, defined as half of the maximum ion diamagnetic frequency in the pedestal region. This diamagnetic frequency, defined as $\omega_i = \frac{n_{\mathrm{tor}}}{e_i\,n_i}\frac{\mathrm{d}p}{\mathrm{d}\psi_N}$ (e_i is the ion charge, n_i is the ion density and p is the total pressure), corresponds to a rotation in the opposite direction of the plasma current and it leads

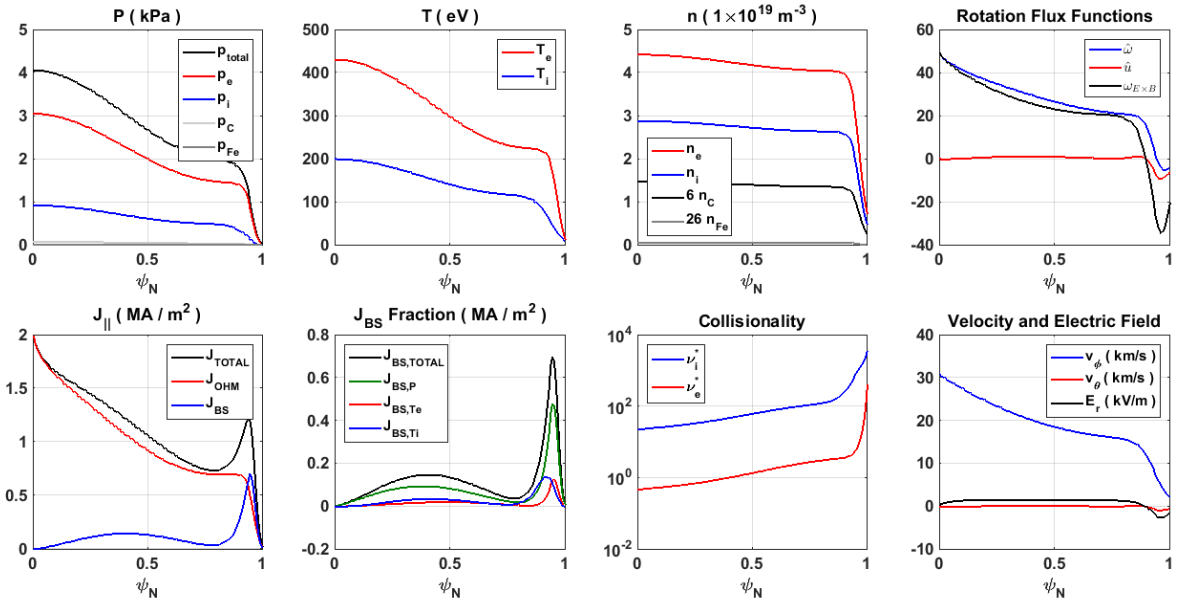

Figure 4.2: Kinetic profiles of the standard scenario.

to stabilisation of MHD modes on the plasma edge [52, 53]. If the normalised growth rate $\gamma/\omega_i^* < 1$, the unstable single-fluid MHD mode is stabilised by the ion diamagnetic rotation and the plasma is considered to be stable. Otherwise, the MHD mode grows faster than the stabilising effect of the ion diamagnetic rotation, leading to a unstable mode and, consequently, to an ELMs.

According to the single-fluid stability calculations shown in Figure 4.3, the unstable MHD modes in the TCABR standard scenario are the ones with $n = 5 - 7$, with $n = 6$ being the most unstable. This results indicates that the standard scenario will be unstable to peeling-ballooning modes, which is highly desirable as the TCABR upgrade aims at further developing methods of ELM suppression using RMP fields. Peeling-ballooning modes are driven by parallel current density flowing on the plasma edge, $J_{\parallel,\text{edge}}$, and the pressure gradient in the plasma edge, $(\boldsymbol{\nabla} p)_{\text{edge}}$.

In addition, a characterisation of the stability of these unstable modes was carried to investigate the role of plasma resistivity, η. A plasma resistivity scan was carried for the most unstable MHD mode of the standard scenario ($n = 6$) to understand whether these unstable modes are of ideal nature or resistive nature.

As shown in Figure 4.4, as the resistivity is reduced to the ideal MHD limit ($\frac{\eta}{\eta_0} \to 0$), the $n = 6$ mode becomes stable, *i.e.* $\gamma < 0$. Therefore, plasma resistivity is expected to play a significant role on the mode growth rate of the TCABR H-mode standard scenario, indicating that ELMs in TCABR will be driven by resistive modes. A further indication is through the growth rate data fitting: the angular coefficient of this log-log graph is 0.322 ± 0.002, close to the theoretically predicted behaviour of resistive modes, *i.e.* $\gamma = \gamma_0(\frac{\eta}{\eta_0})^{1/3}$ [54]. Hence, it is expected that the TCABR standard scenario be unstable to ELMs.

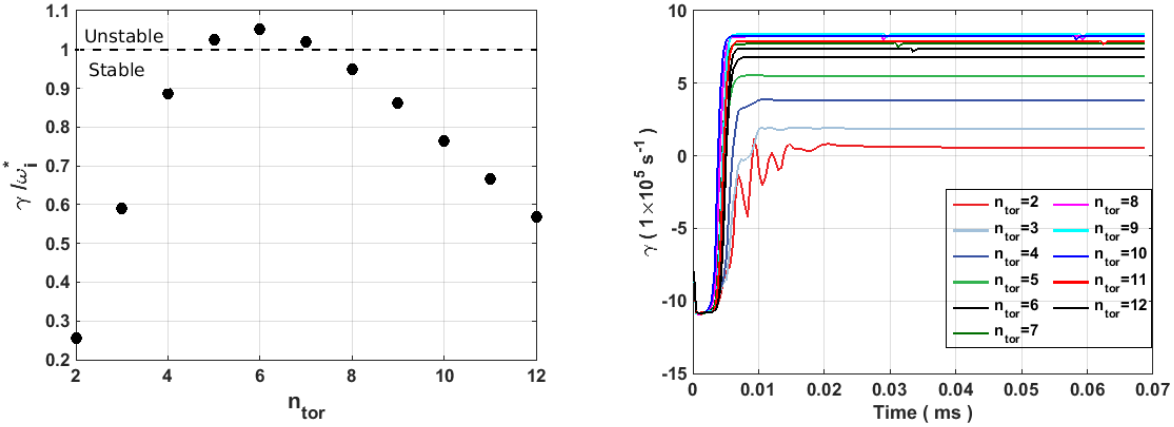

Figure 4.3: Normalised growth rates γ/ω_i^* for MHD modes with toroidal mode numbers $n = 2$ to 12 and the time evolution of the growth rates γ up to $150\,\tau_A$.

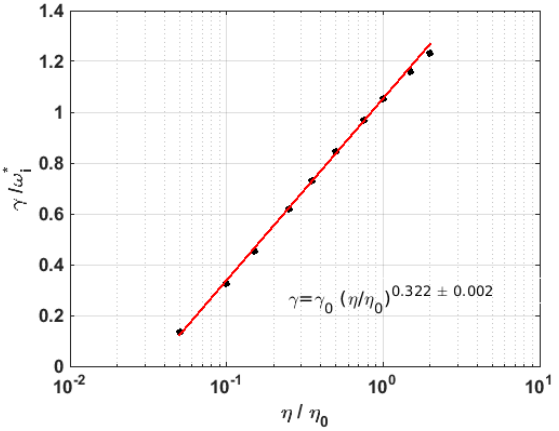

Figure 4.4: Effect of plasma resistivity on the growth rate of the $n = 6$ peeling ballooning mode.

4.3 Pedestal parameters and edge stability analysis

In H-mode, the edge of plasma develops a structure called pedestal in which temperature, density and pressure profiles have a strong gradient. Since H-mode plasmas can be unstable to ELMs triggered by $\boldsymbol{\nabla} p$ and/or $J_\parallel$ on the plasma edge [14, 33], the study of the pedestal height and width is essential to characterise the stability of these plasmas.

In this work, the study of $\boldsymbol{\nabla} p$ and $J_\parallel$ impact on plasma stability was carried out through the simulation of five H-mode scenarios, where all scenarios have the same plasma current $I_p = 112.4$ kA, elongation $\kappa = 1.39$, inferior and superior triangularity $\delta_u = 0.27$, $\delta_l = 1$, minor radius $a = 0.15$ m and density and temperature at R_0 $T_{e,0} = 550\,\text{eV}$, $n_{e,0} = 3.6 \times 10^{19}\,\text{m}^{-3}$. These five scenarios differ in the values of electron temperature at the pedestal top ($T_{\text{e,ped}}$) and electron temperature pedestal width (Δ_{ψ_N}), listed on Table 4.1.

Shot	$T_{\mathrm{e,ped}}$ (eV)	Δ_{ψ_N}
007000	220	0.075
007001	200	0.075
007002	240	0.075
007003	220	0.085
007004	220	0.065

Table 4.1: Prescribed electron temperature on the pedestal top and electron temperature pedestal width studied to investigate stability.

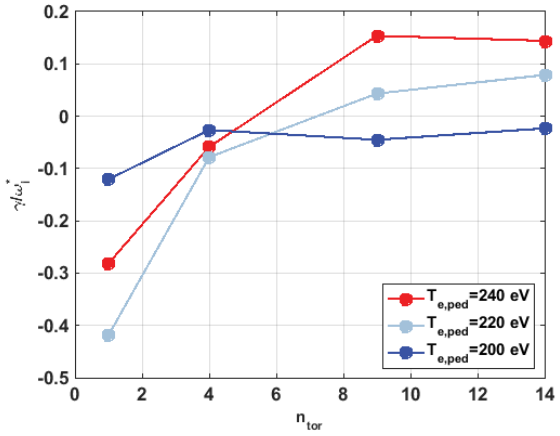

Figure 4.5: Stability analysis of the MHD modes with toroidal mode numbers n = 1, 4, 9, 14 for different pedestal top electron temperature.

The stability calculations of the five TCABR H-mode scenarios was carried out for $n_{\mathrm{tor}} = 1 - 14$, Figure 4.5, and the simulation was carried out for $150\,\tau_A$. The stability analysis was executed through a study about the growth rates of the MHD modes for several values $T_{\mathrm{e,ped}}$ and a fixed value $\Delta_{\psi_N} = 0.075$.

For the low-n_{tor} values ($n_{\mathrm{tor}} = 1,\ 4$), *i.e.* mainly driven by peeling modes, the variation of $T_{\mathrm{e,ped}}$ did not change their stability, showing that this scenarios are not close to the peeling mode stability boundary. It also indicates that the $(J_{\parallel})_{\mathrm{edge}}$ values are not close to the critical stability value. On the other hand, the intermediate and high n_{tor} values ($n_{\mathrm{tor}} = 9,\ 14$) shows that an increase of $T_{\mathrm{e,ped}}$ causes the plasma to become unstable with $n_{\mathrm{tor}} = 14$ mode being the most sensitive to the $T_{\mathrm{e,ped}}$ variation. The mode $n_{\mathrm{tor}} = 9$ and $n_{\mathrm{tor}} = 14$ correspond, respectively, to peeling-ballooning and ballooning modes, in which $\boldsymbol{\nabla} p_{\mathrm{edge}}$ is the main drive. Since an increase of $T_{\mathrm{e,ped}}$ also increases $p_{\mathrm{e,ped}}$, $\boldsymbol{\nabla} p_{\mathrm{edge}}$ also increases for a fixed value of Δ_{ψ_N}, leading to more unstable peeling-ballooning and ballooning modes.

Stability calculations were also carried out to study the effect of variations of Δ_{ψ_N} for a fixed $T_{\mathrm{e,ped}} = 220\,eV$, Figure 4.6.

For low-n_{tor} values ($n_{\mathrm{tor}} = 1,\ 4$), the variation of the pedestal width did not destabilise these modes. Notwithstanding, the intermediate and high-n_{tor} values ($n_{\mathrm{tor}} = 9,\ 14$) shows that an increase of pedestal width causes these MHD modes to become stable, with the

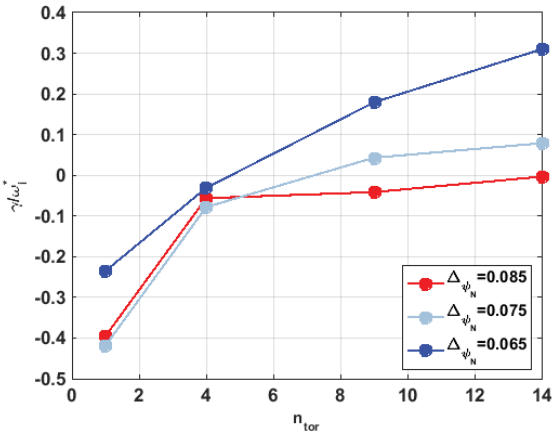

Figure 4.6: Stability analysis of the MHD modes with toroidal mode numbers n = 1, 4, 9, 14 for different pedestal widths.

mode $n = 14$ being the most sensitive to this pedestal width variation. These modes are driven by peeling-ballooning ($n_{\text{tor}} = 9$) and ballooning ($n_{\text{tor}} = 14$) modes, both modes are driven by $\boldsymbol{\nabla} p_{\text{edge}}$, where an increase of Δ_{ψ_N}, for a fixed $T_{\text{e,ped}}$, decreases $(\boldsymbol{\nabla} p)_{\text{edge}}$ and the mode drive, thus having a stabilising effect.

Lastly, the five H-mode scenarios studied showed that current driven modes (peeling modes) are stable and far from the stability boundary. However, peeling-ballooning and ballooning modes are sensitive to $T_{\text{e,ped}}$ and Δ_{ψ_N}, where both quantities change $\boldsymbol{\nabla} p_{\text{edge}}$ and, consequently, the main drive of these modes. The results indicate that numerical simulations of ELMs in TCABR must be done carefully due to the MHD stability modes sensibility to pedestal quantities.

Chapter 5

Conceptual design of an advanced set of RMP coils for TCABR

In this chapter, the physical criteria for the RMP coils study are presented and the geometric design and the current optimisation of 2 coil sets are carried: one coil set on the LFS, called I-coils, and the other on the HFS, called CP-coils. Each coil set is composed of 3 toroidal arrays of 18 equally spaced coils, where each coil is powered independently by a AC/DC current supply. On AC mode, the supply will be able to do any waveform with $f \leq 10$ kHz and current amplitude up to 1 kA, while in DC, the current amplitude can be as high as 2 kA. Each I-coil has 12 turns, while each CP-coil has 30 turns. The baseline RMP model is presented in Figure (5.1).

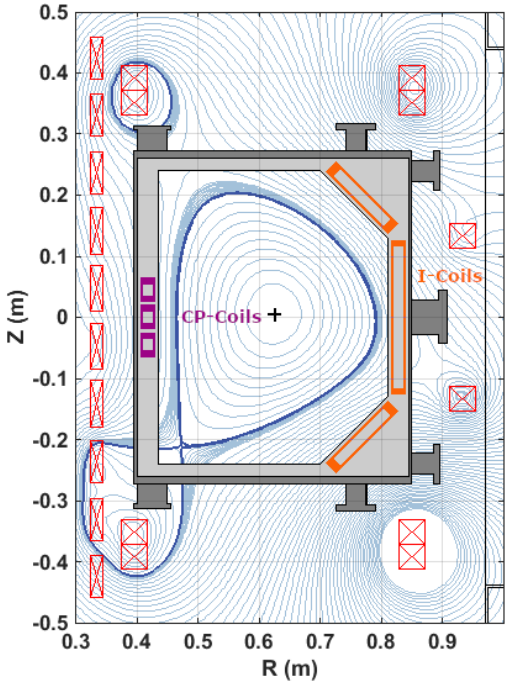

Figure 5.1: The TCABR RMP coil baseline model.

This study is conducted on the coil geometric design and the coil current optimisation in order to reduce the current supplied to the coils. However, the RMP fields produced by these coils need to satisfy a physical criteria set.

5.1 Design criteria

The conceptual design of the TCABR RMP coils requires a set of criteria that is used to evaluate whether the applied RMP fields are perturbing the plasma edge sufficiently to create a layer of stochastic magnetic field lines through the overlap of magnetic islands, induced by the RMP fields. This stochastic layer can mitigate/suppress ELMs by enhancing particle and energy radial transport, thus having a stabilising effect. This mechanism can reduce the amount of energy and particles ejected during an ELM, or even completely suppress ELMs through an increase of the neoclassical turbulence transport [23].

In this work, three design criteria are being considered:

- The magnitude of the magnetic perturbations that are resonant at $\psi_N = 0.95$ must be sufficiently large, *i.e.* [55]:

$$\frac{\delta B_{m,n}}{B_0} \geq 1 \times 10^{-4}, \; i.e. \quad \delta B_{m,n} \geq 0.01\% B_0 \tag{5.1}$$

  where $\delta B_{m,n}$ is the magnitude of Fourier-decomposed RMP field perpendicular to the equilibrium flux surfaces [56]:

$$\delta B_{m,n} = \frac{(2\pi)^2}{A} \int_0^{2\pi} \int_0^{2\pi} \frac{\delta \boldsymbol{B} \cdot \boldsymbol{\nabla} \psi}{\boldsymbol{B} \cdot \boldsymbol{\nabla} \theta^*} \, e^{i(m\theta^* - n\phi)} \, d\theta^* \, d\phi \tag{5.2}$$

  where θ^* is the poloidal angle defined by $d\theta^* = \frac{d\phi}{q}$

- The Chirikov parameter [57, 58, 59] σ_{Chir} must satisfy the following condition in the pedestal region on the vacuum model:

$$\sigma_{\text{Chir}} = \frac{\Delta\psi_{m,n} + \Delta\psi_{m+1,n}}{2(\psi_{m+1,n} - \psi_{m,n})} > 1 \tag{5.3}$$

  where $\Delta\psi_{m,n}$ is the width (in ψ_N units) of a magnetic island located at the rational surface $q(\psi_N) = m/n$.

- The vacuum island overlap width Δ_{VIOW} must be wider than the pedestal width Δ_{ψ_N} [60]:

$$\Delta_{\text{VIOW}} > \Delta_{\psi_N} = 0.08 \tag{5.4}$$

The first criterion corresponds to the minimum RMP field strength needed to create a stochastic layer in the pedestal region. This layer is formed when magnetic islands overlap. The criterion uses the norm Fourier-decomposed component rather than the magnitude of

the field, since only the resonant component $\delta B_{m,n}$ can open magnetic islands on rational surfaces $q(\psi_N) = m/n$.

The second criterion addresses the island overlap. The Chirikov parameter is a figure of merit which depends on the width of neighbour magnetic islands and the distance between their rational surfaces. The criterion says if $\sigma_{\text{Chir}} > 1$, two neighbouring magnetic islands boundaries would overlap, breaking the island structure and creating a region of stochastic magnetic field lines. Furthermore, to avoid the plasma core to slow down, exiting from H-mode and locking in phase with the perturbation field, and the discharge to end in a major current disruption, this criterion must be only satisfied in the pedestal region. Therefore, the Chirikov parameter must not be larger than one in the plasma core region.

The third criterion is related to the aforementioned criterion, but now all of the magnetic island widths are analysed thoroughly, verifying if a chain of magnetic islands are overlapping and creating the stochastic region in the pedestal region [60].

Another important study carried out in this work is the coil current optimisation for a given equilibrium configuration and coil set. In this case, the goal is to minimise the coil currents needed to satisfy the physical criteria (Equations 5.1 to 5.4). Using an optimal coil current configuration reduced the demand on the power supplies. The RMP coil current is modelled as:

$$I_{\text{coil}}(t) = I_{\text{RMP}}(t)\cos[n_{\text{tor}}\phi + \phi_0(t)] \tag{5.5}$$

where $I_{\text{RMP}}(t)$ is the current amplitude, n_{tor} is the toroidal periodicity of the coil current distribution, ϕ is the toroidal coordinate and $\phi_0(t)$ is the phase of the coil current.

One advantage of this current model is the ability to change the coil current configuration n_{tor} and the perturbative magnetic field spectra by adding ϕ_0 values on different coil arrays. The focus of this coil current optimisation study is, for a given coil configuration n_{tor}, to find the values of ϕ_0 on the upper and lower arrays of I- and CP-coils that minimises the coil current while verifying if the physical criteria.

Since the power supplies planned for the RMP coils will be able to work on AC and DC current modes, both $I_{\text{RMP}}(t)$ and $\phi_0(t)$ can be time-dependent quantities and will be able to be adjusted and controlled in real time during a discharge. In this work, both quantities are taken as constant in time, since the focus is on the coil design and optimisation. The plasma scenario used for the coil design is the standard scenario described at section 4.1.

5.2 The I-coils

In this section, it is discussed the optimisation of the RMP coil sets on the LFS. Firstly, a coil current minimisation is carried for the baseline coil geometry, verifying if the criteria, given by Equations 5.1 to 5.4, are satisfied. Secondly, a coil geometry optimisation is executed, where three coil geometries are investigated. Finally, a coil current minimisation of the optimal coil geometry is carried out.

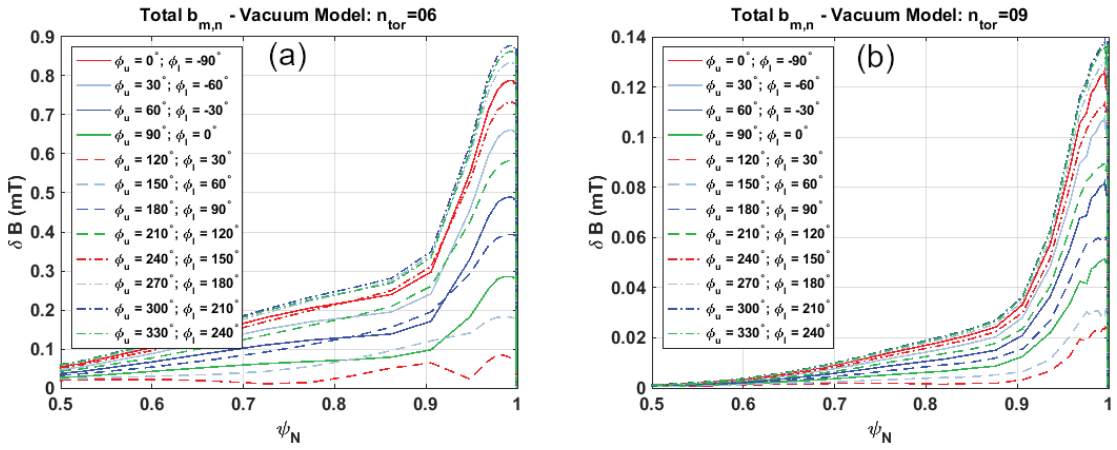

Figure 5.2: Radial profile of the amplitude of the resonant harmonics for different values of toroidal phase and for (a) $n_{\rm tor} = 6$ and (b) $n_{\rm tor} = 9$.

5.2.1 Optimisation of the coil current configuration

The design of the I-coils starts with an optimisation of the coil current configuration for the baseline I-coils shown in Figure (5.1). The optimisation of the coil current configuration consists of an independent scan of the toroidal phase ϕ_0 (Equation 5.5) of the current configuration in the upper and in the lower I-coil arrays relative to the middle I-coil array. These independent scans aim at identifying the minimum current amplitude in each coil of the three I-coil toroidal arrays that create resonant harmonics in the pedestal region while meeting all the design criteria for $n_{\rm tor} \leq 9$. In these calculations, the current amplitude in the three toroidal arrays is set to the maximum value that can be provided by the power supplies, *i.e.* $I_{\rm RMP} = 24$ kA-t. While the middle array toroidal phase $\phi_0 = 0$, the upper and lower arrays have toroidal phases given by ϕ_u and ϕ_l, respectively.

As shown in Figure 5.2, for both $n_{\rm tor}$, the optimal toroidal phase for the upper array is $\phi_u = 300°$ and for the lower array is $\phi_l = 210°$. While the criterion given by Equation 5.1 is well satisfied for the $n_{\rm tor} = 6$ configuration, for which the peak resonant field at $\psi_N = 0.95$ is 0.7 mT (0.05% of B_0), it is marginally satisfied for the $n_{\rm tor} = 9$ configuration, for which the peak resonant field at $\psi_N = 0.95$ is 0.1 mT (0.01% of B_0).

In addition to the calculated resonant harmonic, which was used to verify the design criteria given by Equation 5.1, magnetic island widths and both the associated Chirikov parameter and the vacuum overlap island width (VIOW) were calculated to verify the design criteria given by Equations 5.3 and 5.4. Using the optimal coil current configurations for $n_{\rm tor} = 6$ and $n_{\rm tor} = 9$ and applying the maximum current amplitude $I_{\rm RMP} = 24$ kA-t, the magnetic islands and their widths were calculated for both plasma models, namely the vacuum approach the single-fluid MHD model, Figure 5.3.

From Figure (5.3), the RMP fields on both $n_{\rm tor}$ configurations show that the island overlap criterion (Equation 5.4) is satisfied, with the remark that for the $n_{\rm tor} = 9$ configuration, the design criteria is marginally satisfied. The calculations for the $n_{\rm tor} = 6$ configuration also demonstrates that, at the maximum $I_{\rm RMP}$, the island overlap region extends over the pedestal and into the plasma, which is not desirable, as this reduces

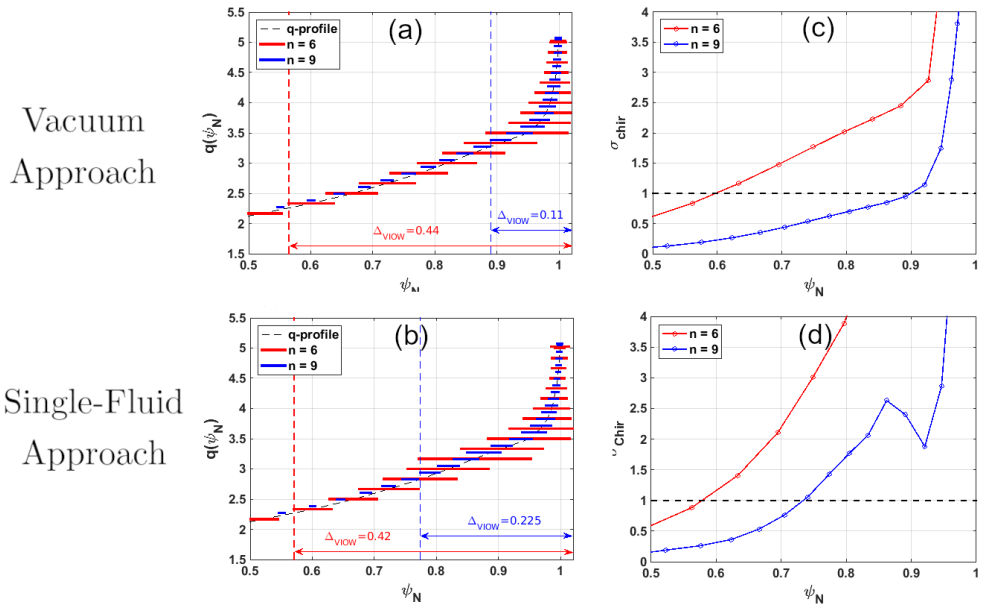

Figure 5.3: (a-b) Magnetic island width and (c-d) Chirikov parameter for the optimal current for $n_{\text{tor}} = 6$ and $n_{\text{tor}} = 9$ and for both plasma models.

plasma confinement. This is an indication that the maximum value of I_{RMP} that can be provided by the power supplies is sufficiently large to create a stochastic layer in the plasma edge and have a significant impact on ELM stability.

When the single-fluid plasma response is accounted, the calculated island widths and both the associated Chirikov parameter and Δ_{VIOW} are significantly affected. For example, the magnetic islands in the pedestal region for both n_{tor} configurations are wider than the islands on the vacuum approach on the pedestal top ($0.8 < \psi_N < 0.9$), where the effect can be observed in the Chirikov parameter for both n_{tor} and on the Δ_{VIOW} for the $n_{\text{tor}} = 9$. This shows that the plasma that is amplifying the intermediate and high-n_{tor} fields, which is a very fortunate result as it enforces the amplitude of the weaker, higher-n_{tor} harmonics, which are the ones that suffer stronger radial decay.

To further characterise these observations, magnetic field lines were traced to generate Poincaré sections that allow to visualise the stochastic layer in the plasma edge. This technique allows us to visualise the magnetic island structure and the assessment of the plasma reaction to the RMP fields applied by the I-coils. Using optimal current configuration, Poincaré sections were generated for both plasma models for $n_{\text{tor}} = 6$, Figure 5.4, and for $n_{\text{tor}} = 9$, Figure 5.5.

The calculations show that, as already expected, that an increase in the coil current I_{RMP} increases the stochastic layer. Note that a well noticeable edge stochastic layer width is produced with relatively low values of coil current (the maximum current amplitude is $\text{I}_{\text{RMP}} = 24\,\text{kA-t}$). It is somewhat surprising that the Poincaré sections presented in Figure 5.4 suggest that the plasma response increases significantly the width of the stochastic layer for $n_{\text{tor}} = 6$, while the results presented in Figure 5.3 indicate that plasma response should not have a significant effect. Note, however, in Figure 5.3(b) and (d), the presence

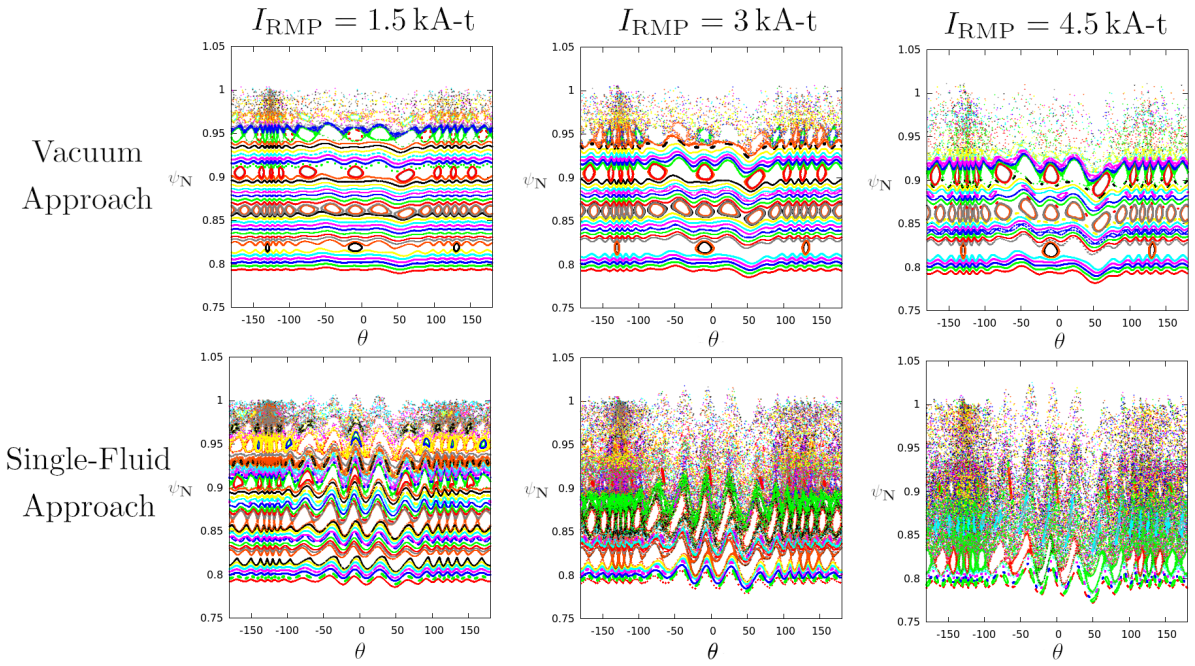

Figure 5.4: Poincaré sections for optimal current configuration and $n_{\mathrm{tor}} = 6$.

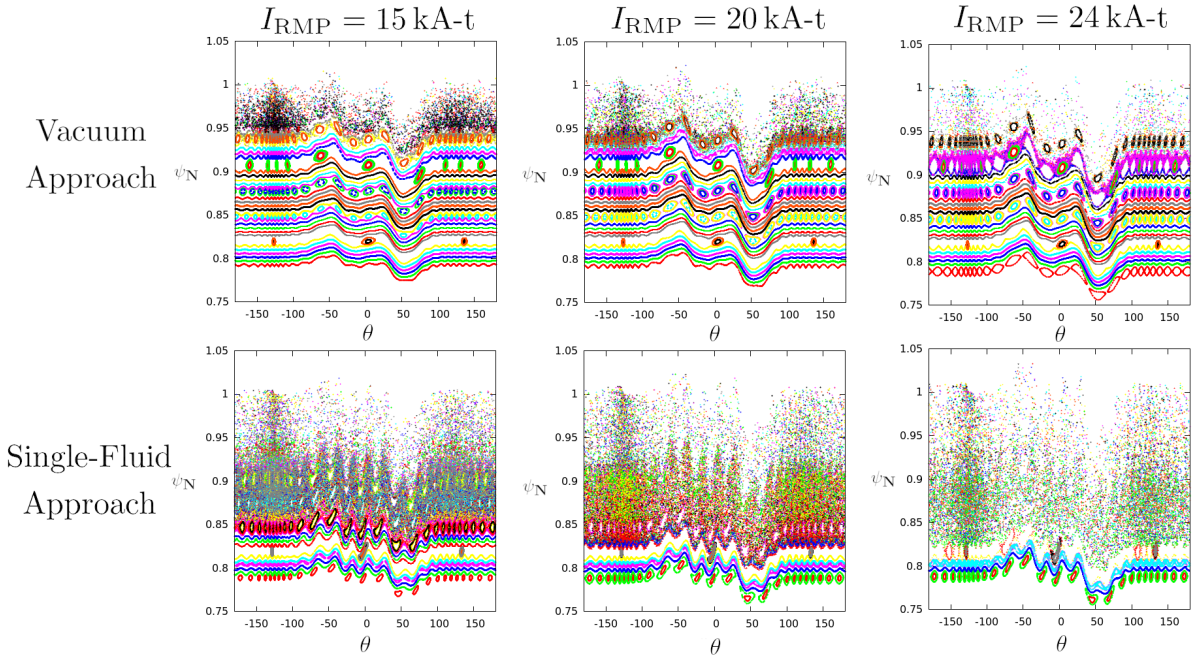

Figure 5.5: Poincaré sections for optimal current configuration and $n_{\mathrm{tor}} = 9$.

of an region of larger stochasticity around $\psi_N = 0.85$ when plasma response is taken into account. Apparently, this non-monotonic increase of stochasticity towards the plasma edge is the cause of the observed, and desired, increase of the stochastic layer width.

Regarding the $n_{\text{tor}} = 9$ configuration, it is quite easy to see in Figure 5.5 that plasma response has a stronger effect when compared with the $n_{\text{tor}} = 6$. This result is in agreement with the previous observation that plasma response is expected to amplify RMP field of higher values of n_{tor}. This seems to be one of the few situations in which nature appear to provide an impact that goes in the desired direction as higher-n_{tor} RMP fields are the ones the decay more rapidly with the distance from the coil due to their $1/r^{n_{\text{tor}}}$ dependence. Of course, one should be very careful with this very optimistic predictions since plasma response models, such as the one implemented in the M3D-C^1 code used in this work, are still under an intense process of validation. Therefore, future experiments will have to be carefully carried out on TCABR to provide an answer about to which extent these optimistic predictions are trustful.

5.2.2 Optimisation of the coil geometry

As presented in section 5.2.1, a more conservative analysis (vacuum approach) shows that the amplitude of the resonant fields for $n_{\text{tor}} = 9$ marginally satisfies the design criteria. To improve the design of the I-coils, the geometry of the coils were optimised such that the RMP field amplitudes for $n_{\text{tor}} = 9$ be sufficiently large to well satisfy the design criteria. For this study, three coil geometries were considered, Figure 5.6, and the optimal coil current toroidal phases found in section 5.2.1 for $n_{\text{tor}} = 6$ and $n_{\text{tor}} = 9$ were used, *i.e.* upper array coils $\phi_u = 300°$ and lower array coils $\phi_l = 210°$. The calculated resonant harmonics for $n_{\text{tor}} = 6$ and $n_{\text{tor}} = 9$, for $\text{I}_{\text{RMP}} = 24\,\text{kA-t}$ and for both plasma models, can be seen in Figure 5.7. In this study, the middle I-coil array was switched off to study the effect of geometry optimisation only on the upper and lower I-coil arrays.

The calculations show that the coil geometry #3 is the optimal design, one that produces the largest RMP fields, for both $n_{\text{tor}} = 6$ and $n_{\text{tor}} = 9$ and for the same coil current amplitude, ($\text{I}_{\text{RMP}} = 24\,\text{kA-t}$), being about two times larger than the amplitude produced by the other coil geometries. In the vacuum approach, the RMP fields produced by the upper and lower coil arrays for $n_{\text{tor}} = 6$ and $n_{\text{tor}} = 9$ satisfy the design criterion given by Equation 5.1: at $\psi_N = 0.95$, the RMP fields for $n_{\text{tor}} = 6$ are $0.95\,\text{mT}$ (which is 0.079% of B_0) and for $n_{\text{tor}} = 9$, the RMP fields are $0.17\,\text{mT}$ (which is 0.014% of B_0). This result shows that, even without using the middle array, the geometry #3 I-coils are capable of producing RMP fields that well satisfy the design criteria, given by Equation 5.1, for both n_{tor}.

Furthermore, when plasma response is taken into account, all three coil geometries studied produced the same plasma response pattern, indicating that the plasma response to perturbations applied from the LFS is not sensitive to the location and geometry of the I-coils.

An interesting observation is the correlation between plasma amplification of resonant harmonics and the $\omega_{\boldsymbol{E}\times\boldsymbol{B}}$ plasma rotation profile, Figure 4.2. The regions where the gradient of the $\omega_{\boldsymbol{E}\times\boldsymbol{B}}$ is close to 0 are also the regions where the RMP fields are amplified.

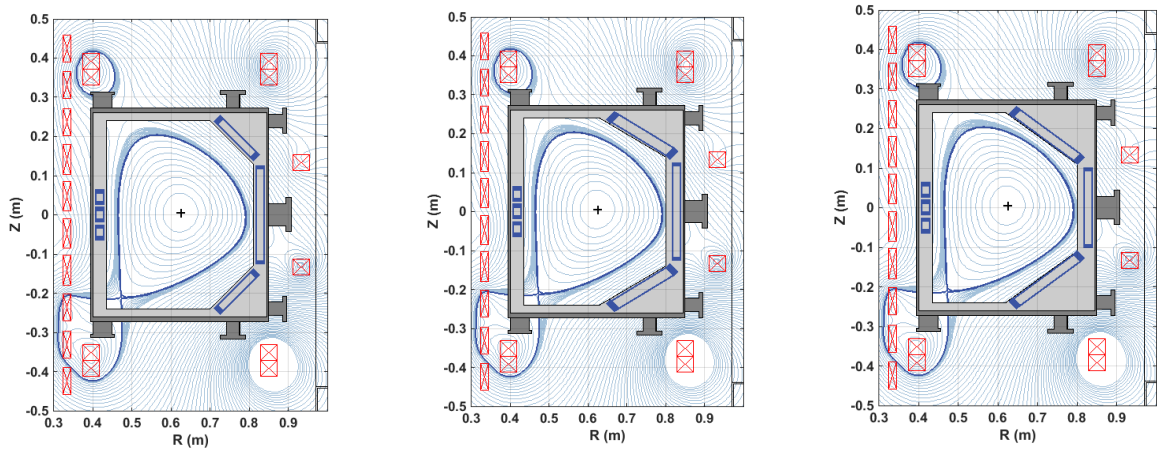

(a) Coil geometry 1 - baseline (b) Coil geometry 2 (c) Coil geometry 3

Figure 5.6: Different geometries of the I-coils upper and lower arrays that were studied in this geometric optimisation.

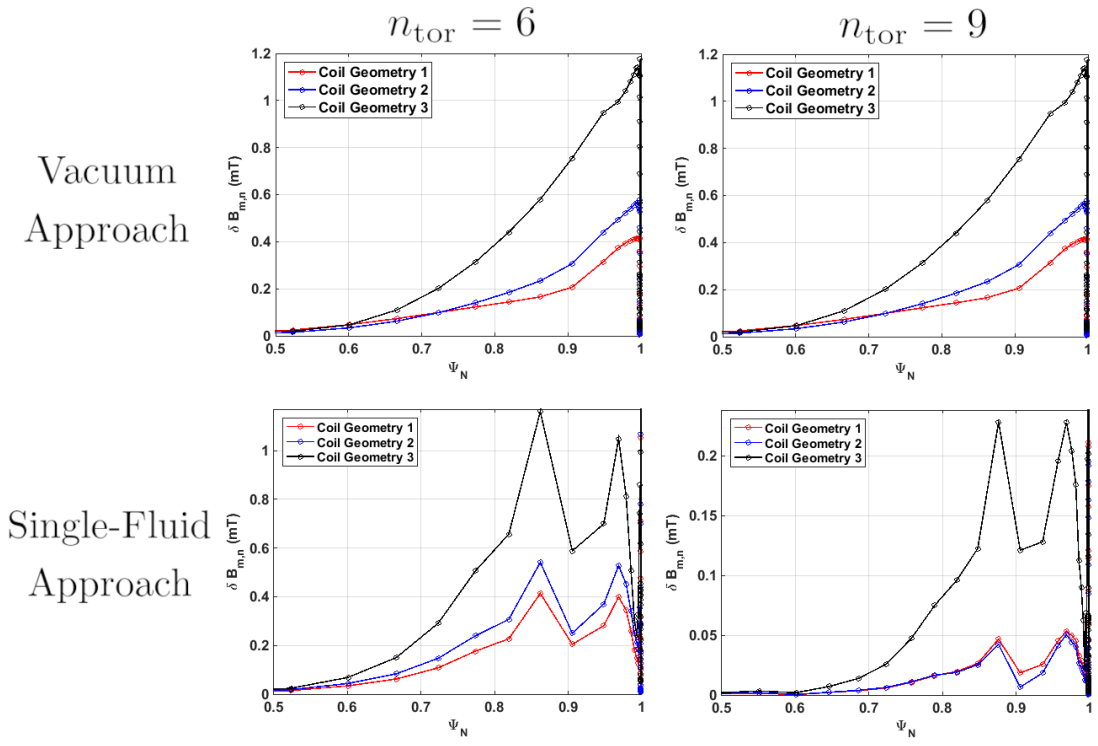

Figure 5.7: Radial profile of the amplitude of the resonant harmonics for different coil geometries, n_{tor} configurations and plasma models.

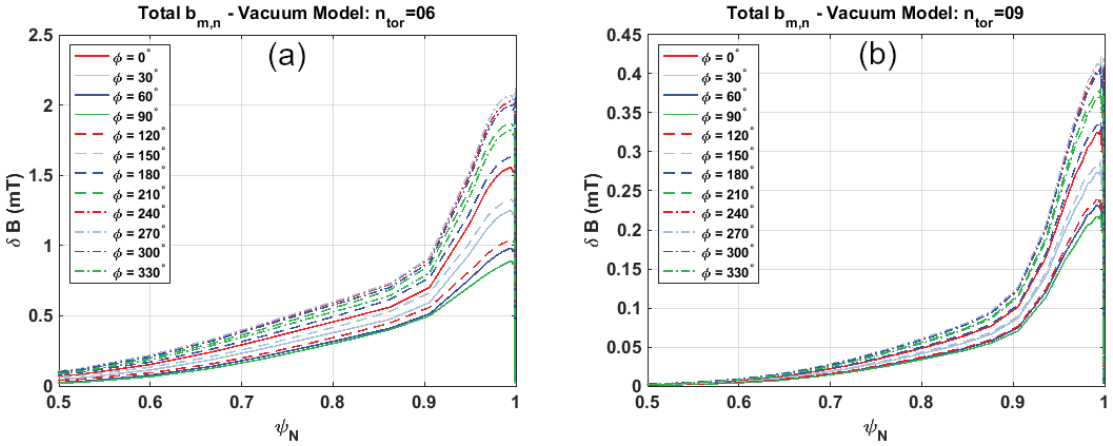

Figure 5.8: Radial profile of the amplitude of the resonant harmonics for different values of toroidal phase and for (a) $n_{\text{tor}} = 6$ and (b) $n_{\text{tor}} = 9$.

On the other hand, the regions where the gradient of the $\omega_{\boldsymbol{E}\times\boldsymbol{B}}$ is large are also the regions where the RMP fields are screened. The same kind of correlation was also seen in M3D-C^1 simulations for NSTX-U single-null and snowflake scenarios [61]. This observation implies that the plasma response is very sensitive to the plasma rotation radial profile and, therefore, due to the complexity of measuring plasma rotation accurately, this might be a source of discrepancy between simulated plasma response and experimental measurements of plasma response.

5.2.3 The optimised conceptual design

The coil geometry #3 had the best performance using the coil current configuration optimised for the coil geometry #1, which was the baseline geometry. Therefore, a better characterisation of this new geometry requires an additional optimisation of the coil current configuration. Once more, this optimisation was carried out by scanning the toroidal phase ϕ_0 on the upper and lower arrays relative to the middle array. This scan was done in a *symmetric* configuration, where the upper and lower arrays have the same toroidal phase value. The scan was carried out for $n_{\text{tor}} = 6$ and $n_{\text{tor}} = 9$ configuration with maximum current amplitude ($\text{I}_{\text{RMP}} = 24$ kA-t) and for both plasma models.

As shown in Figure 5.8, for both n_{tor}, the optimal toroidal phase ϕ_0 for the upper and lower arrays are 270°. With this value, the RMP fields produced by the coil geometry #3 satisfied the design criteria, given by Equation 5.1, for the vacuum approach: at $\psi_N = 0.95$, the RMP fields for $n_{\text{tor}} = 6$ configuration are 1.55 mT (0.13% of B_0) and the RMP fields for $n_{\text{tor}} = 9$ are 0.27 mT (0.02% of B_0). These results correspond to a two times increase for $n_{\text{tor}} = 6$ and a three times increase for $n_{\text{tor}} = 9$. Therefore, the optimisation of the coil geometry and the current configuration allowed a significant reduction on the coil current I_{RMP} amplitude that must be provided by the power supplies.

The calculations of magnetic island widths was repeated in order to verify if the Δ_{VIOW} criterion, Equation 5.4, and the Chirikov criterion, Equation 5.3, were met, Figure 5.9.

In the vacuum approach, the magnetic island overlap and the Chirikov criteria, Equa-

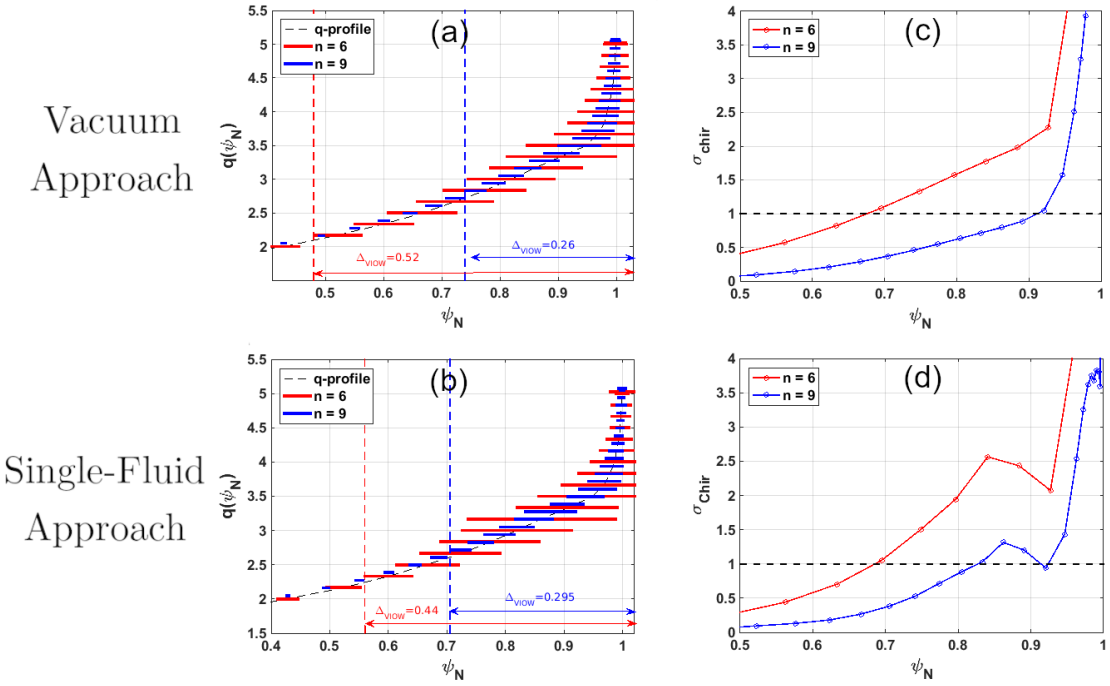

Figure 5.9: (a-b) Magnetic island width and (c-d) Chirikov parameter for the optimal current for $n_{\text{tor}} = 6$ and $n_{\text{tor}} = 9$ and for both plasma models.

tions 5.4 and 5.3, are both well satisfied. Using the maximum coil current $I_{\text{RMP}} = 24$ kA-t, the magnetic island overlap region reaches the plasma core ($\psi_N < 0.8$) for both $n_{\text{tor}} = 6$ and $n_{\text{tor}} = 9$. Therefore, 24 kA-t is more than enough to produce significant amplitudes of $n_{\text{tor}} = 6$ perturbations in the plasma edge.

In the single-fluid model, the plasma is found to shield $n_{\text{tor}} = 6$ RMP fields in the plasma core, while the plasma is modestly amplifying the $n_{\text{tor}} = 9$ RMP fields at the pedestal top. The plasma amplification/screening effect can be seen more easily on the Chirikov parameter for the single-fluid model, where this behaviour was also seen coil geometry #1.

A further analysis about the magnetic islands was carried out by tracing the magnetic field lines and generating Poincaré section for both vacuum approach and single-fluid model for $n_{\text{tor}} = 6$, Figure 5.10, and $n_{\text{tor}} = 9$, Figure 5.11.

Similarly to the baseline coil geometry #1, when the single-fluid plasma response is taken into account, the calculated island widths and both the associated Chirikov parameter and the Δ_{VIOW} are significantly affected. For $n_{\text{tor}} = 6$, the magnetic island structure is severely destroyed for $I_{\text{RMP}} = 1.5$ kA-t and 3 kA-t and, for $I_{\text{RMP}} = 4.5$ kA-t, the stochastic region extends deeper into the plasma ($\psi_N > 0.75$) for current amplitudes as low as $\text{I}_{\text{RMP}} = 4.5$ kA-t. For $n_{\text{tor}} = 9$, stochastic region also increases due to the plasma response but does not extend so deep into the plasma core as the $n_{\text{tor}} = 6$. However, a comparison between single-fluid model $n_{\text{tor}} = 9$ from coil geometry #3 and the baseline coil geometry, Figure 5.5, shows that a large decrease in the I_{RMP} was possible, going from $\text{I}_{\text{RMP}} = 15$ kA-t for the baseline coil geometry to $\text{I}_{\text{RMP}} = 6$ kA-t for the coil geometry #3.

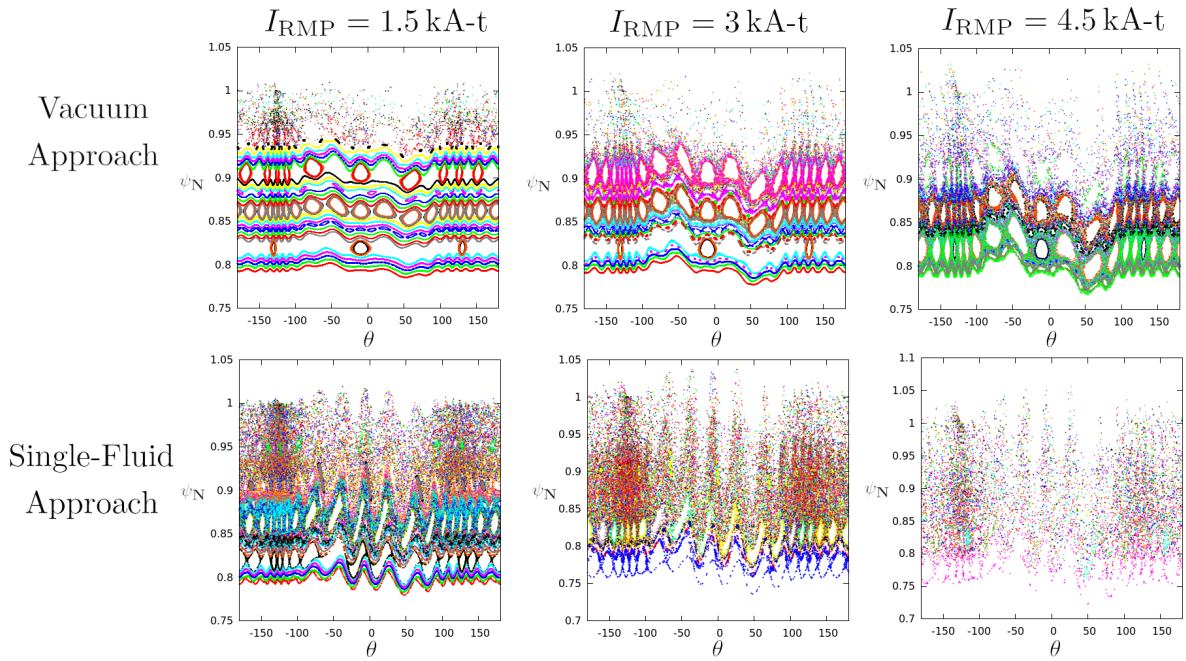

Figure 5.10: Poincaré sections for optimal current configuration and $n_{\mathrm{tor}} = 6$.

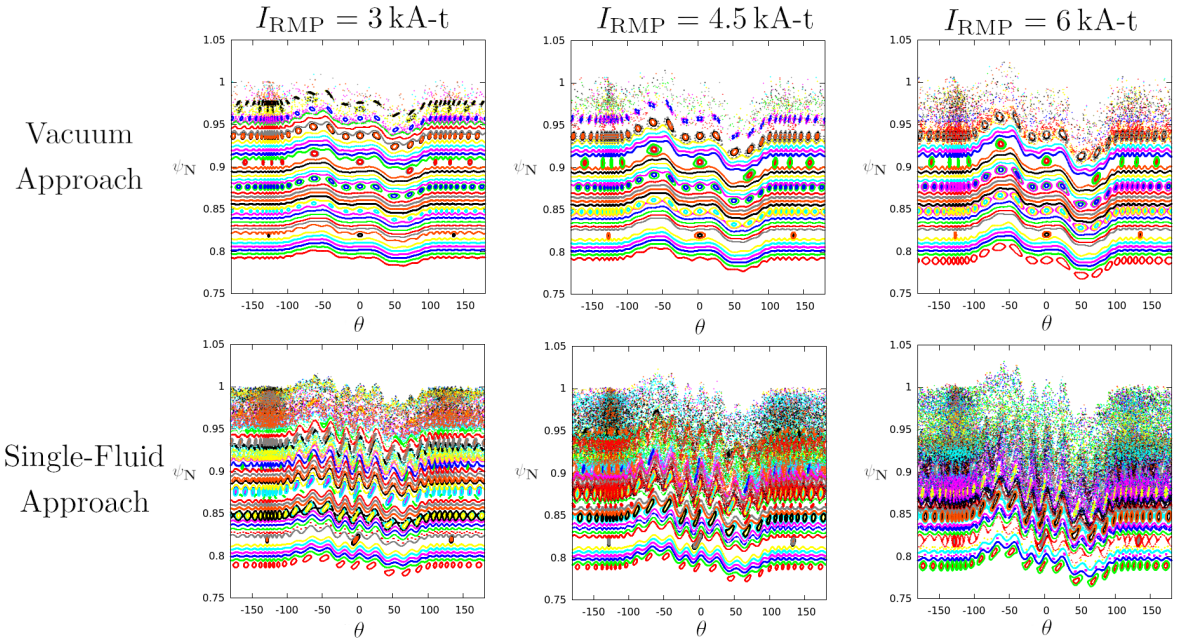

Figure 5.11: Poincaré sections for optimal current configuration and $n_{\mathrm{tor}} = 9$.

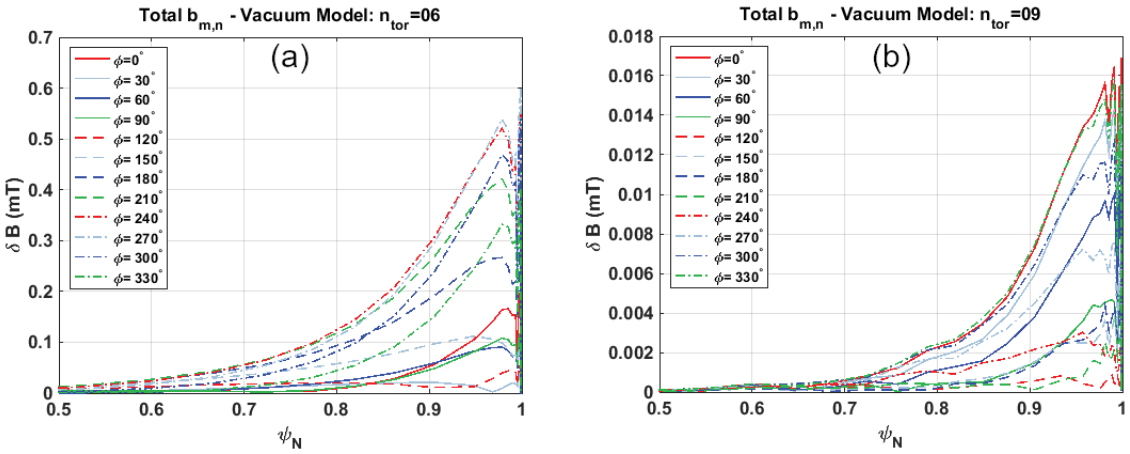

Figure 5.12: Radial profile of the amplitude of the resonant harmonics for different values of toroidal phase and for (a) $n_{\text{tor}} = 6$ and (b) $n_{\text{tor}} = 9$.

In summary, the results presented demonstrated that the coil geometry #3 satisfied the design criteria to mitigate/suppress ELMs for $n_{\text{tor}} \leq 9$ current configurations.

5.3 The CP-coils

In this section, it is discussed the optimisation of the RMP coil sets on the HFS. Firstly, a coil current minimisation is carried for the baseline coil geometry, verifying if the criteria, given by Equations 5.1 to 5.4, are satisfied. Secondly, a coil geometry optimisation is executed, where several coil geometries are investigated.

5.3.1 Optimisation of the coil current configuration

Analogously to the conceptual design of the I-coils, the conceptual design of the CP-coils will be made first through the optimisation of the CP-coils current configuration for the baseline coil geometry shown in Figure 5.1 and for both $n_{\text{tor}} = 6$ and $n_{\text{tor}} = 9$. This optimisation was carried out with the maximum coil current amplitude $\text{I}_{\text{RMP}} = 60$ kA-t and the toroidal phase was scanned in a *antisymmetric* configuration, where the upper and lower arrays have opposite phases, *e.g.* if the upper array has $\phi_u = 90°$, the lower array will have $\phi_l = -90°$.

Calculations of the resonant harmonics in the vacuum approach for $n_{\text{tor}} = 6$, Figure 5.12(a) show that the optimal toroidal phase corresponds to $\phi_u = 270°$ and $\phi_l = -270°$. In this optimal toroidal phase, the RMP fields produced for $n_{\text{tor}} = 6$ well satisfy the criterion given by Equation 5.1 in the vacuum approach: at $\psi_N = 0.95$, the RMP fields amplitude are 0.45 mT, which are 0.037% of B_0. For $n_{\text{tor}} = 9$, the optimal toroidal phase is found to be $\phi_u = \phi_l = 0°$. The calculations show that, for $n_{\text{tor}} = 9$, the design criteria are not satisfied: at $\psi_N = 0.95$, the RMP fields amplitude are 0.013 mT, which are 0.0011% of B_0. This value is a factor 10 smaller than that required for ELM suppression in other machines. Therefore, additional optimisation is required. It is important to note

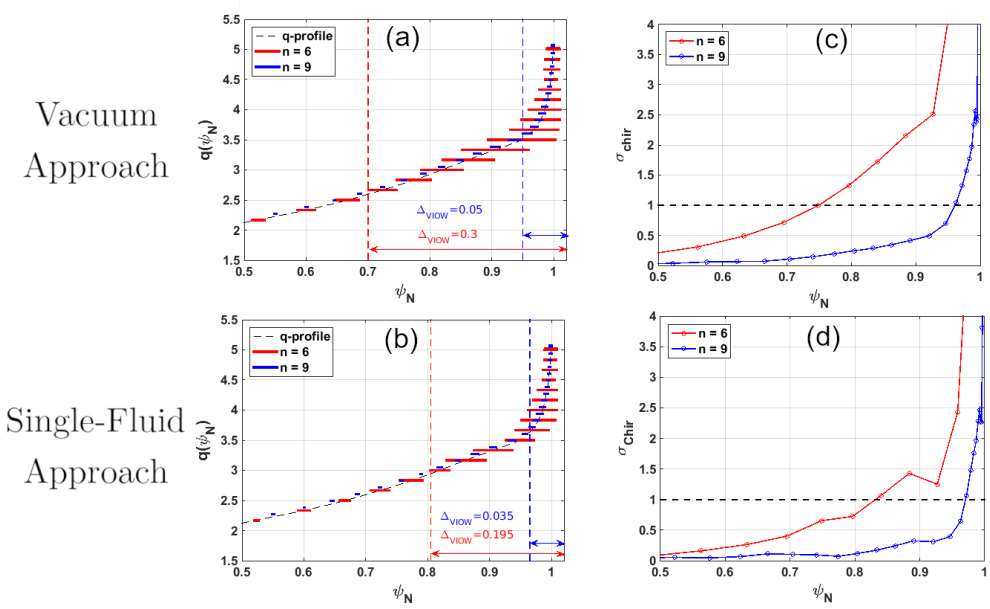

Figure 5.13: (a-b) Magnetic island width and (c-d) Chirikov parameter for the optimal current for $n_{\text{tor}} = 6$ and $n_{\text{tor}} = 9$ and for both plasma models.

that the design criteria used in this work correspond to a set of empirical laws obtained from experiments in which the RMP fields are applied from the LFS. There is evidence, however, that RMP fields applied from the HFS can couple more efficiently with the plasma and, interestingly, the optimal applied field pitch is significantly different of the equilibrium field pitch [62].

Using the optimal toroidal phase for both $n_{\text{tor}} = 6$ and $n_{\text{tor}} = 9$, magnetic islands overlap, Equation 5.4, and the Chirikov criteria, Equation 5.3, were studied for both plasma models, Figure 5.13.

The calculations show that, in the vacuum approach, only the optimal $n_{\text{tor}} = 6$ configuration satisfies the magnetic island overlap condition, Equation 5.4, and the Chirikov condition, Equation 5.3. With maximum coil current amplitude $\text{I}_{\text{RMP}} = 60$ kA-t, the overlap region is wider than the pedestal, even being able to reach the plasma core, with the Chirikov parameter satisfying the criterion in the pedestal region. The optimal $n_{\text{tor}} = 9$ configuration, on the other hand, creates a stochastic region just in a fraction of the pedestal.

When the plasma response is taken into account, the RMP fields applied by the CP-coils are screened by the plasma, reducing the magnetic island, the Chirikov parameter, Δ_{VIOW} and, consequently, the stochastic layer width. This is the opposite behaviour observed for I-coils simulations, where the plasma is found to amplify the applied RMP fields. One should note, however, that in these simulations of the CP-coils the low-n_{tor} harmonic is more shielded than the high-n_{tor} harmonic, while for the I-coils the high-n_{tor} harmonic is amplified by the plasma.

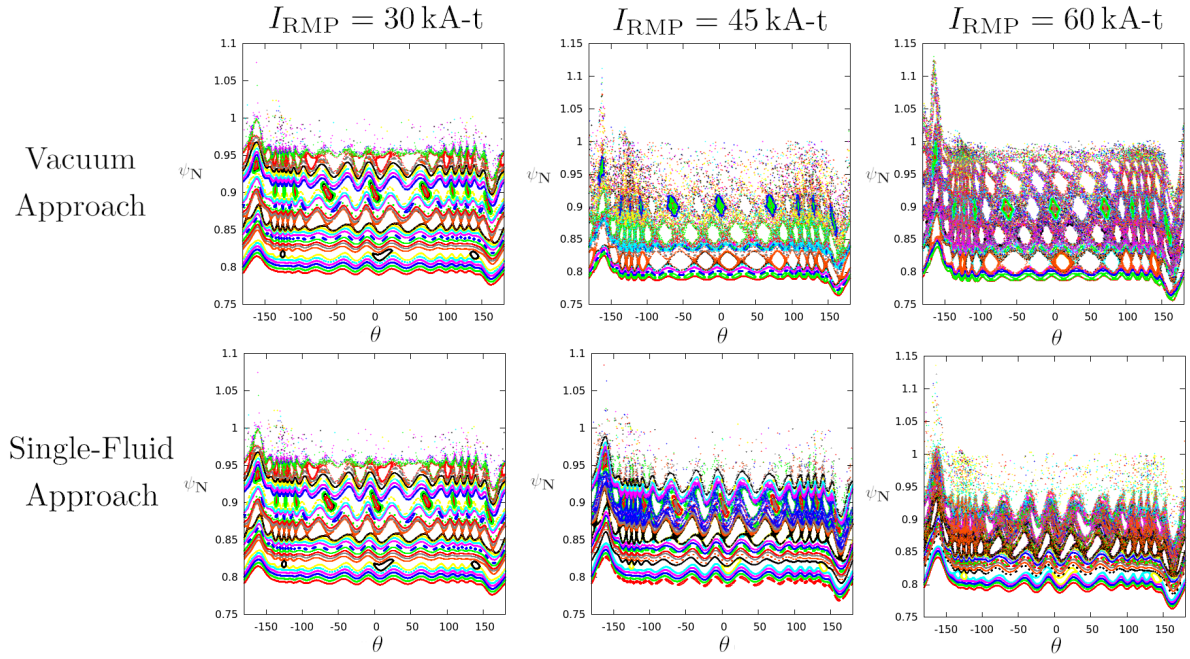

Figure 5.14: Poincaré sections for optimal current configuration and $n_{\mathrm{tor}} = 6$.

Although these results show that a further optimisation of the CP-coils is required, they also show that the plasma response to fields applied from the LFS and from the HFS can be quite different. The physical mechanisms that control if an particular harmonic will be screened or amplified are still not clear and require more detailed study.

In order to better understand how the plasma response is changing the RMP fields applied from the HFS, Poincaré section were created for both $n_{\mathrm{tor}} = 6$, Figure 5.14, and $n_{\mathrm{tor}} = 9$, Figure 5.15, for both plasma models.

The calculations show that, for $n_{\mathrm{tor}} = 6$, the stochastic layer width increases when the current amplitude increases, which is, of course, expected, and when the plasma response is taken into account. This last observation is opposite to the observed reduction of Δ_{VIOW} and $\sigma_{\mathrm{Chir}} = 1$ criteria presented above. One possible explanation to this apparent inconsistency is the non-monotonic increase in island width towards the plasma edge, where a local maximum can be seen at about $\psi_N = 0.88$. For $n_{\mathrm{tor}} = 9$ and in agreement with the calculated magnetic island overlap criteria, the calculations shows very little or almost no difference between the vacuum and single-fluid approach.

In summary, the results show that the baseline CP-coils geometry can create $n_{\mathrm{tor}} = 6$ RMP fields, although the current amplitude $\mathrm{I_{RMP}}$ must be close to 60 kA-t limit. Nonetheless, for $n_{\mathrm{tor}} = 9$, the calculations using both plasma models show that the design criteria are not satisfied. A factor of 10 in the RMP amplitude is needed to satisfy the design criteria, hence a geometry optimisation of the CP-coils is required.

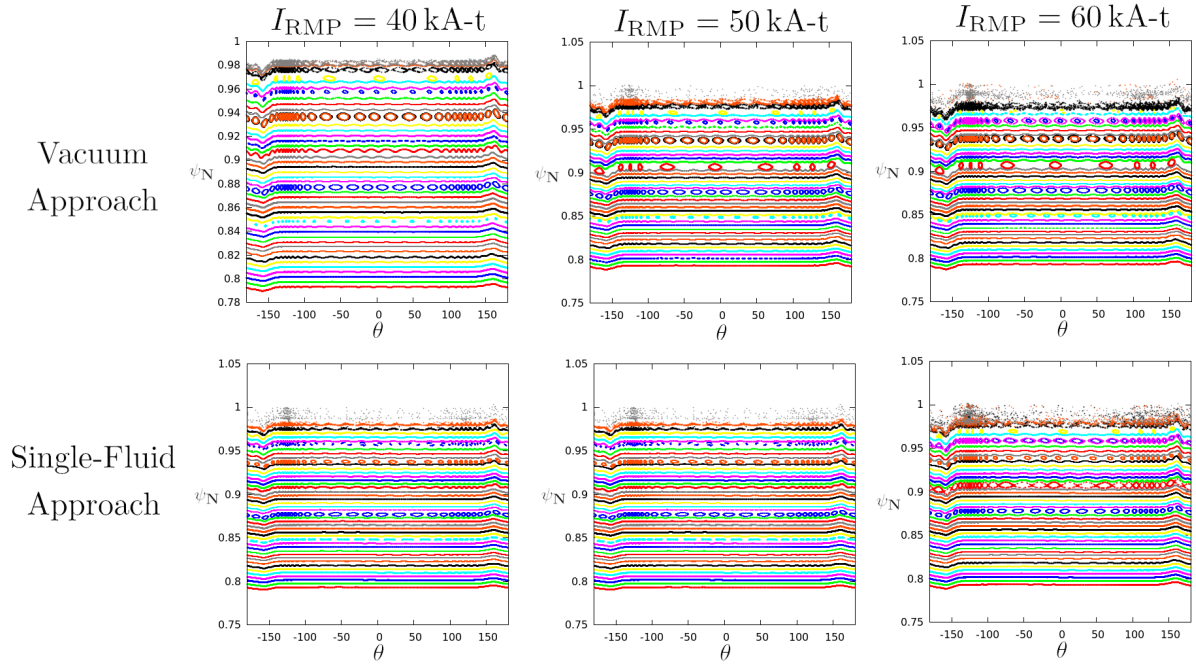

Figure 5.15: Poincaré sections for optimal current configuration and $n_{\mathrm{tor}} = 9$.

5.3.2 Optimisation of the coil geometry

As presented in the previous subsection, even at the maximum current amplitude, the $n_{\mathrm{tor}} = 9$ fields do not satisfy the design criteria and, therefore, a geometric optimisation is required. In this geometry optimisation, the CP-coils height and array separation are scanned for the optimal toroidal phase found in section 5.3.1. In the coil height scan, the height of the CP-coils was varied from 3 cm up to 11 cm while keeping the distance between coil arrays to 2 cm. The middle array was fixed at $z = 0$.

The calculations show that optimal CP-coils height is about 5 cm, Figure 5.16, where the value of the RMP fields at $\psi_N = 0.95$ are 0.014 mT (0.0011% of B_0). This value, however, is still not enough to satisfy the design criteria. To further improve the coil design, the distance between coil arrays was scanned from 1 cm up to 7 cm, while the coil height was fixed at its optimal value, *i.e.* 5 cm. The scan results are presented in Figure 5.17.

The calculation show that the optimal distance between coil arrays is 2 cm, which is exactly the one used in the height scan, *i.e.* there is no way to improve the coil design even further. However, there is still one possibility of increasing the resonant fields very significantly without requiring further geometric changes in the coils. The calculations shown in this work were carried out with the plasma separatrix being about 6 cm away from the coils. Since the RMP field amplitude depends on the distance between the coils and the plasma as $1/d^{n_{\mathrm{tor}}}$, a small reduction of the distance between the plasma and CP-coils is expected to have a very significant positive impact. However, this distance scan study would require the creation of various plasma scenarios, with fine-tuned distances between the coils and the plasma, thus, this study will be carried out in another work.

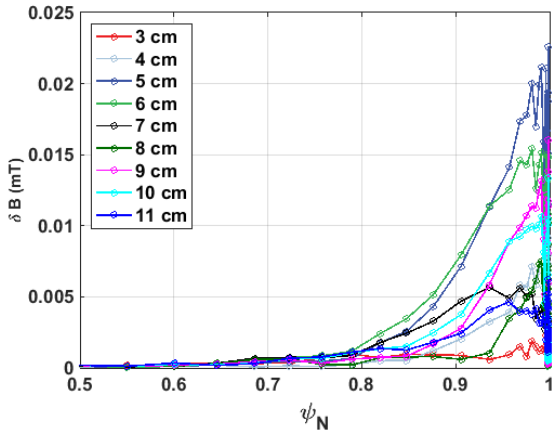

Figure 5.16: CP-coils design height tested in $n_{\text{tor}} = 9$ configuration where the plasma is in the vacuum approach.

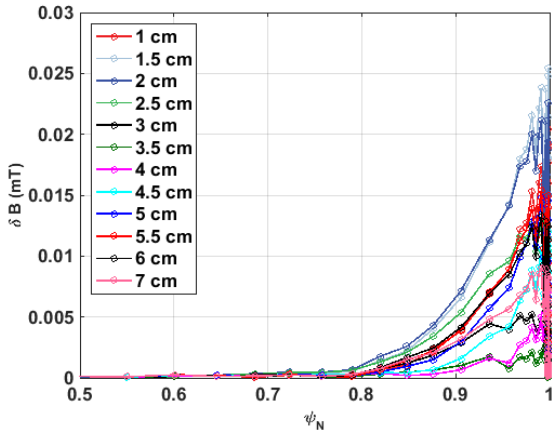

Figure 5.17: CP-coils design distance between arrays tested in $n_{\text{tor}} = 9$ configuration where the plasma is in the vacuum approach.

Anyway, the expected improvement in RMP field amplitude can be estimated as:

$$\frac{\delta B_{m,n=9}(d = 3\,\text{cm})}{\delta B_{m,n=9}(d = 6\,\text{cm})} = \left(\frac{6\,\text{cm}}{3\,\text{cm}}\right)^9 \approx 500. \tag{5.6}$$

Therefore, a small change in the plasma radial position can lead to an increase in RMP field amplitude of more than two orders of magnitude. This strong variation of the amplitude of RMP fields of higher-n_{tor} values with the distance from the plasma poses a challenge to the plasma control system, which will have to be at the same time robust and precise in order to keep the plasma horizontal position very stable to avoid excessively large variations of resonant field amplitude during experiments.

Chapter 6

Conclusions

In this work, H-mode kinetic plasma equilibria were generated and their stability were analysed with the visco-resistive MHD code M3D-C^1. The simulations showed that TCABR ohmic H-mode plasmas are expected to be unstable to ELM whose most unstable modes have $n_{\text{tor}} = 6 - 8$. In addition, these modes were found to be resistive, *i.e.* their growth rates are expected to be very sensitive to the electron temperature profile during experiments. Due to this expected sensitivity, the effect of the pedestal structure on the modes growth rate was studied through variations of the electron temperature pedestal width and height. The results show that the unstable resistive peeling-ballooning modes in TCABR will have a dominant ballooning drive.

After characterising the equilibrium and stability of the envisaged H-mode standard plasma scenario in TCABR, the conceptual design of an advanced set of ELM control coils was carried out using the so-called vacuum approach and the M3D-C^1 visco-resistive single-fluid MHD model. For the conceptual design, the coils were separated into two groups: the LFS coils (I-coils) and the HFS coils (CP-coils). The design of the I-coils was carried out through the optimisation of the geometry of the coils and of the toroidal phase of the coil currents in the upper and lower arrays. The RMP field amplitudes predicted in both plasma models were large enough to satisfy the design criteria for $n_{\text{tor}} \leq 9$. However, while the design of the CP-coils followed the same procedure carried out for the I-coils, the RMP field amplitudes for $n_{\text{tor}} = 9$ were not enough to satisfy the design criteria, being a factor 10 smaller than the minimum required. The RMP field amplitudes for $n_{\text{tor}} = 6$ were marginally satisfied. Although the coils design is fully optimised, there is still the possibility of bringing the plasma closer to the coils. Decreasing the distance between the plasma separatrix and the CP-coils from 6 cm to 3 cm is expected to increase the RMP field amplitude by a factor 500, making the RMP fields to be a factor 50 larger than the minimum required by the design criteria. This study, however, is left for a separate work due to the need of generating a large variety of well-tuned plasma scenarios.

It is important to note that the design criteria used in this work correspond to a set of empirical laws obtained from experiments in which the RMP fields are applied from the LFS. There is evidence, however, that RMP fields applied from the HFS can couple more efficiently with the plasma and, interestingly, with the optimal applied field pitch being significantly different from the equilibrium field pitch [62].

One very interesting observation is that, on the one hand, RMP fields of high-n_{tor} values were amplified by the plasma when the perturbations are applied from the LFS. On the other hand, low-n_{tor} harmonics are screened by the plasma when the perturbations are applied from the HFS. Although these results are somewhat problematic for the CP-coils, whose fields suffer from a strong radial decay, they also show that the plasma response to fields applied from the LFS and from the HFS can be quite different. Another interesting observation is the correlation between plasma response amplification of the RMP field and the $\omega_{\boldsymbol{E}\times\boldsymbol{B}}$ plasma rotation radial profile. The regions where the gradient of $\omega_{\boldsymbol{E}\times\boldsymbol{B}}$ is close to zero are also the regions where the RMP fields are amplified. On the other hand, the regions where the gradient of the $\omega_{\boldsymbol{E}\times\boldsymbol{B}}$ profile is large are also the regions where the RMP fields are screened. This observation implies that the plasma response is very sensitive to the plasma rotation radial profile and, therefore, due to the complexity of measuring plasma rotation accurately, this might be a source of discrepancy between simulated plasma response and experimental measurements of plasma response. The physical mechanisms that control if a particular harmonic will be screened or amplified are still not clear and require a more detailed study.

Bibliography

[1] H. Zohm. *Magnetohydrodynamic Stability of Tokamaks*. Wiley-VCH, 1st edition, 2015.

[2] R. Groebner *et al.* Role of neutrals in density pedestal formation in DIII-D. *Plasma Physics and Controlled Fusion*, 44:A265, 04 2002.

[3] U.S. Department of Energy. International Energy Outlook (July 2013). *U.S. Energy Information Administration*, 2013. http://www.eia.gov/forecasts/ieo/index.cfm.

[4] International Energy Agency. World Energy Outlook (November 2013). *U.S. Energy Information Administration*, 2013. http://www.worldenergyoutlook.org/publications/weo-2013/.

[5] D.J.C. MacKay. Sustainable Energy - without the hot air. *UIT Cambridge Ltd*, 2009. http://www.inference.phy.cam.ac.uk/sustainable/book/tex/cft.pdf.

[6] J.A. Wesson. *Tokamaks*. Clarendon Press, Oxford, 2^{th} Edition, 1997.

[7] J.P. Freidberg. *Plasma Physics and Fusion Energy*. Cambridge University Press, London, 2007.

[8] L.A. Artsimovich. Tokamak devices. *Nuclear Fusion*, 12(2):215, 1972. http://stacks.iop.org/0029-5515/12/i=2/a=012.

[9] L.A. Artsimovich *et al.* Experiments in tokamak devices. 3^{rd} *International Conference on Plasma Physics and Controlled Fusion Research*, 1:157, 1968.

[10] J.D Lawson. Some criteria for a power producing thermonuclear reactor. *Proceedings of the Physical Society. Section B*, 70(1):6, 1957. http://stacks.iop.org/0370-1301/70/i=1/a=303.

[11] H. Zohm. Edge localized modes (ELMs). *Plasma Physics and Controlled Fusion*, 38(2):105–128, 1996. https://doi.org/10.1088%2F0741-3335%2F38%2F2%2F001.

[12] J.W. Connor *et al.* Magnetohydrodynamic stability of tokamak edge plasmas. *Physics of Plasmas*, 5, 1998. https://aip.scitation.org/doi/abs/10.1063/1.872956.

[13] J.R. Ferron *et al.* Modification of high mode pedestal instabilities in the DIII-D tokamak. *Physics of Plasmas*, 7, 2000. https://aip.scitation.org/doi/abs/10.1063/1.874053.

[14] P.B. Snyder *et al.* Characterization of peeling–ballooning stability limits on the pedestal. *Plasma Physics and Controlled Fusion*, 46, 2004. http://iopscience.iop.org/article/10.1088/0741-3335/46/5A/014/meta.

[15] H.R. Wilson *et al.* Magneto-hydrodynamic stability of the H-mode transport barrier as a model for edge localized modes: an overview. *Plasma Physics and Controlled Fusion*, 48, 2006. http://iopscience.iop.org/article/10.1088/0741-3335/48/5A/S06/meta.

[16] A. Loarte *et al.* Characteristics of type I ELM energy and particle losses in existing devices and their extrapolation to ITER. *Plasma Physics and Controlled Fusion*, 45, 2003. http://iopscience.iop.org/article/10.1088/0741-3335/45/9/302/meta.

[17] T.E. Evans. Resonant magnetic perturbations of edge-plasmas in toroidal confinement devices. *Plasma Physics and Controlled Fusion*, 57(12):123001, 2015. https://doi.org/10.1088%2F0741-3335%2F57%2F12%2F123001.

[18] Iter organization. http://www.iter.org/.

[19] A. Loarte *et al.* Progress on the application of ELM control schemes to ITER scenarios from the non-active phase to DT operation. *Nuclear Fusion*, 54, 2014. http://iopscience.iop.org/article/10.1088/0029-5515/54/3/033007/meta.

[20] A W Degeling *et al.* Magnetic triggering of ELMs in TCV. *Plasma Physics and Controlled Fusion*, 45(9):1637–1655, aug 2003.

[21] L D Horton *et al.* ITER-relevant h-mode physics at ASDEX upgrade. *Plasma Physics and Controlled Fusion*, 46(12B):B511–B525, nov 2004.

[22] P.T Lang *et al.* ELM frequency control by continuous small pellet injection in ASDEX upgrade. *Nuclear Fusion*, 43(10):1110–1120, sep 2003.

[23] T. E. Evans, R. A. Moyer, P. R. Thomas, J. G. Watkins, T. H. Osborne, J. A. Boedo, E. J. Doyle, M. E. Fenstermacher, K. H. Finken, R. J. Groebner, M. Groth, J. H. Harris, R. J. La Haye, C. J. Lasnier, S. Masuzaki, N. Ohyabu, D. G. Pretty, T. L. Rhodes, H. Reimerdes, D. L. Rudakov, M. J. Schaffer, G. Wang, and L. Zeng. Suppression of Large Edge-Localized Modes in High-Confinement DIII-D Plasmas with a Stochastic Magnetic Boundary. *Physical Review Letters*, 92(23):235003, June 2004.

[24] Harold Grad and Hanan Rubin. Hydromagnetic equilibria and force-free fields. *Journal of Nuclear Energy (1954)*, 7(3):284–285, 1958.

[25] V D Shafranov. Equilibrium of a toroidal plasma in a magnetic field. *Journal of Nuclear Energy. Part C, Plasma Physics, Accelerators, Thermonuclear Research*, 5(4):251–258, jan 1963.

[26] H. Lütjens, A. Bondeson, and O. Sauter. The CHEASE code for toroidal MHD equilibria. *Computer Physics Communications*, 97(3):219–260, 1996.

[27] A.A. Ivanov *et al.* The spider code - solution of direct and inverse problems for free boundary tokamak plasma equilibrium. *Keldysh Institute Preprints*, 39:1–24, 2009.

[28] G Szepesi, L C Appel, N C Hawkes, M Sertoli, and D Terranova. Advanced equilibrium reconstruction for JET with EFIT++. *47th EPS Conference on Plasma Physics*, page 4, 2021.

[29] L.L. Lao *et al.* Equilibrium analysis of current profiles in tokamaks. *Nuclear Fusion*, 30(6):1035–1049, 1990.

[30] J.-M. Moret *et al.* Tokamak equilibrium reconstruction code LIUQE and its real time implementation. *Fusion Engineering and Design*, 91:1–15, 2015.

[31] J. Friedberg. *Ideal Magnetohydrodynamics*. Plenum Press, New York, 1987.

[32] I. B. Bernstein, E. A. Frieman, Martin David Kruskal, R. M. Kulsrud, and Subrahmanyan Chandrasekhar. An energy principle for hydromagnetic stability problems. *Proceedings of the Royal Society of London. Series A. Mathematical and Physical Sciences*, 244(1236):17–40, 1958.

[33] P.B. Snyder, N. Aiba, M. Beurskens, R.J. Groebner, L.D. Horton, A.E. Hubbard, J.W. Hughes, G.T.A. Huysmans, Y. Kamada, A. Kirk, C. Konz, A.W. Leonard, J. Lönnroth, C.F. Maggi, R. Maingi, T.H. Osborne, N. Oyama, A. Pankin, S. Saarelma, G. Saibene, J.L. Terry, H. Urano, and H.R. Wilson. Pedestal stability comparison and ITER pedestal prediction. *Nuclear Fusion*, 49(8):085035, August 2009.

[34] P.B. Snyder, R.J. Groebner, J.W. Hughes, T.H. Osborne, M. Beurskens, A.W. Leonard, H.R. Wilson, and X.Q. Xu. A first-principles predictive model of the pedestal height and width: development, testing and ITER optimization with the EPED model. *Nuclear Fusion*, 51(10):103016, October 2011.

[35] J.E Kinsey, G Bateman, T Onjun, A.H Kritz, A Pankin, G.M Staebler, and R.E Waltz. Burning plasma projections using drift-wave transport models and scalings for the H-mode pedestal. *Nuclear Fusion*, 43(12):1845–1854, December 2003.

[36] P B Snyder and H R Wilson. Ideal magnetohydrodynamic constraints on the pedestal temperature in tokamaks. *Plasma Physics and Controlled Fusion*, 45(9):1671–1687, September 2003.

[37] Y. B. Kim, P. H. Diamond, and R. J. Groebner. Neoclassical poloidal and toroidal rotation in tokamaks. *Physics of Fluids B: Plasma Physics*, 3(8):2050–2060, 1991.

[38] A. Ashourvan *et al.* Validation of the kinetic-turbulent-neoclassical theory for edge intrinsic rotation in DIII-d. *Physics of Plasmas*, 25(5):056114, 2018.

[39] J.E. Rice *et al.* Inter-machine comparison of intrinsic toroidal rotation in tokamaks. *Nuclear Fusion*, 47(11):1618–1624, 2007.

[40] O. Sauter *et al.* Neoclassical conductivity and bootstrap current formulas for general axisymmetric equilibria and arbitrary collisionality regime. *Physics of Plasmas*, 6(7):2834–2839, 1999. http://scitation.aip.org/content/aip/journal/pop/6/7/10.1063/1.873240.

[41] ITER Physics Expert Groups on Confinement and Transport *et al.* Chapter 2: Plasma confinement and transport. *Nuclear Fusion*, 39(12), 1999. https://iopscience.iop.org/article/10.1088/0029-5515/39/12/302.

[42] F. Wagner *et al.* Regime of improved confinement and high beta in neutral-beam-heated divertor discharges of the asdex tokamak. *Phys. Rev. Lett.*, 49:1408–1412, 1982.

[43] Y Andrew *et al.* Edge ion parameters at the L–H transition on JET. *Plasma Physics and Controlled Fusion*, 46(2):337–347, 2003.

[44] T. N. Carlstrom *et al.* Evidence for the role of velocity shear on the L-H transition in DIII-D. *Plasma Physics and Controlled Fusion*, 44(5A):A333–A339, 2002.

[45] Y R Martin and TCV team. Synchronization of L-mode to H-mode transitions on the sawtooth cycle in ohmic TCV plasmas. *Plasma Physics and Controlled Fusion*, 46(5A):A77–A85, 2004.

[46] R J Akers *et al.* Transport and confinement in the mega ampère spherical tokamak (MAST) plasma. *Plasma Physics and Controlled Fusion*, 45(12A):A175–A204, 2003.

[47] Y R Martin and TCV team. H-mode threshold power in TCV ohmic plasmas. *Plasma Physics and Controlled Fusion*, 44(5A):A143–A150, 2002.

[48] C. Bush *et al.* H-mode threshold and dynamics in the national spherical torus experiment. *Physics of Plasmas*, 10(5):1755–1764, 2003.

[49] E.J. Doyle (Chair Transport Physics), W.A. Houlberg (Chair Confinement Da Modelling), Y. Kamada (Chair Pedestal Edge), , V. Mukhovatov (co-Chair Transport Physics), T.H. Osborne (co-Chair Pedestal Edge), , A. Polevoi (co-Chair Confinement Da Modelling), G Bateman, J.W Connor, J.G. Cordey (retired), T Fujita, X Garbet, T.S Hahm, L.D Horton, A.E Hubbard, F Imbeaux, F Jenko, J.E Kinsey, Y Kishimoto, J Li, T.C Luce, Y Martin, M Ossipenko, V Parail, A Peeters, T.L Rhodes, J.E Rice, C.M Roach, V Rozhansky, F Ryter, G Saibene, R Sartori, A.C.C Sips, J.A Snipes, M Sugihara, E.J Synakowski, H Takenaga, T Takizuka, K Thomsen, M.R Wade, H.R Wilson, ITPA Transport Physics Topical Group, ITPA Confinement Database and Model Group, and ITPA Pedestal and Edge Topical Group. Chapter 2: Plasma confinement and transport. *Nuclear Fusion*, 47(6):S18–S127, June 2007.

[50] N. M. Ferraro, S. C. Jardin, and P. B. Snyder. Ideal and resistive edge stability calculations with M3D-C1. *Physics of Plasmas*, 17(10):102508, October 2010.

[51] N.M. Ferraro and S.C. Jardin. Calculations of two-fluid magnetohydrodynamic axisymmetric steady-states. *Journal of Computational Physics*, 228(20):7742–7770, November 2009.

[52] N. Aiba *et al.* Impact of rotation and ion diamagnetic drift on MHD stability at edge pedestal in quiescent h-mode plasmas. *Nuclear Fusion*, 60(9):092005, 2020.

[53] P.B. Snyder, R.J. Groebner, J.W. Hughes, T.H. Osborne, M. Beurskens, A.W. Leonard, H.R. Wilson, and X.Q. Xu. A first-principles predictive model of the pedestal height and width: development, testing and ITER optimization with the EPED model. *Nuclear Fusion*, 51(10):103016, October 2011.

[54] G T.A. Huysmans, J P Goedbloed, and W Kerner. Free boundary resistive modes in tokamaks. *Physics of Fluids B*, 5(5), 1993.

[55] T E Evans. Resonant magnetic perturbations of edge-plasmas in toroidal confinement devices. *Plasma Physics and Controlled Fusion*, 57(12):123001, December 2015.

[56] M.J. Schaffer *et al.* Study of in-vessel nonaxisymmetric ELM suppression coil concepts for ITER. *Nuclear Fusion*, 48(2):024004, 2008. https://doi.org/10.1088%2F0029-5515%2F48%2F2%2F024004.

[57] B.V. Chirikov. Resonance processes in magnetic traps. *Journal of Nuclear Energy. Part C, Plasma Physics, Accelerators, Thermonuclear Research*, 1(4):253–260, 1960. https://doi.org/10.1088%2F0368-3281%2F1%2F4%2F311.

[58] S.S. Abdullaev *et al.* On description of magnetic stochasticity in poloidal divertor tokamaks. *Physics of Plasmas*, 15(4):042508, 2008. https://aip.scitation.org/doi/abs/10.1063/1.2907163.

[59] S.S. Abdullaev. *Magnetic Stochasticity in Magnetically Confined Fusion Plasmas: sections 8.2 and 8.3*. Springer, New York, 2014.

[60] M. E. Fenstermacher, T. E. Evans, T. H. Osborne, M. J. Schaffer, M. P. Aldan, J. S. deGrassie, P. Gohil, I. Joseph, R. A. Moyer, P. B. Snyder, R. J. Groebner, M. Jakubowski, A. W. Leonard, and O. Schmitz. Effect of island overlap on edge localized mode suppression by resonant magnetic perturbations in DIII-D. *Physics of Plasmas*, 15(5):056122, 2008.

[61] G.P. Canal *et al.* M3D-C1 simulations of the plasma response to RMPs in NSTX-U single-null and snowflake divertor configurations. *Nuclear Fusion*, 57(7):076007, 2017. https://doi.org/10.1088%2F1741-4326%2Faa6e10.

[62] C. Paz-Soldan *et al.* Observation of a multimode plasma response and its relationship to density pumpout and edge-localized mode suppression. *Physical Review Letters*, 114(10):105001, 2015.